UNIVERSITY OF CALIFORNIA

Los Angeles

Mechanobiology tools for phenotypic studies of cancer

A dissertation submitted in partial satisfaction of the
requirements for the degree Doctor of Philosophy
in Bioengineering

by

Harsha Madan Kittur

2017

ABSTRACT OF THE DISSERTATION

Mechanobiology tools for phenotypic studies of cancer

by

Harsha Madan Kittur
Doctor of Philosophy in Bioengineering
University of California, Los Angeles 2017
Professor Dino Di Carlo, Chair

Recent advances in analyzing cancer genes, proteins, and metabolites have produced a vast library of biomarkers to understand, diagnose, and treat cancer. To add to this library, direct measurement of a cell's phenotypic response to environmental stimuli gives rise to physical biomarkers that may be more indicative of physiological behavior. This dissertation discusses the relevance of physical biomarkers in understanding, diagnosing, and enriching cancer cells, along with the corresponding techniques for doing so. The next chapter goes in depth into a tool that analyzes molecular abnormalities in aneuploid cancer cells that divide in mechanically confined environments. The following chapter discusses another tool that fingerprints breast cancer cells by their “relative adhesive signature” as a potential for diagnosing and predicting metastasis.

The dissertation of Harsha Madan Kittur is approved.

Amy Catherine Rowat

Min Yu

Song Li

Dino Di Carlo, Committee Chair

University of California, Los Angeles

2017

DEDICATION

I would like to dedicate this dissertation...

To my loving mother and father, who brought me up on the principles of hard work, tenacity, and self-improvement.

To my supportive advisor Dino Di Carlo, who inspired me and the rest of the group with his patience, leadership, and quest for knowledge.

To all of my lab mates whose positive personalities cultivated a synergistic environment that was conducive to learning and discovery.

To my fellow HSSRP facilitators James Che, Luke Shaw, Sara Azzam, and our fearless leader William Herrera, whose dedication, empathy, and selflessness enabled us to make significant strides in building a research-intensive summer program for high school students. But I can't stop here without acknowledging the energy that each of our summer students brought to the table, from 2012 through 2016.

To our EGSA team for re-energizing the engineering graduate community and for continuing to be a strong presence on campus.

To this quote by Jim Rohn: “We are the average of the five people we spend the most time with”. For my time at UCLA, I'll pick these 5: Janay Kong, James Che, Mayank Jog, Avery Hua, and Luke Shaw. Who could ask for a better support system than these people?

Contents

ACKNOWLEDGEMENTS

Chapter 1 contains the unpublished work: Kittur, H. and Di Carlo, D. Physical Biomarkers Review (in preparation). HK wrote the manuscript. HK and DD revised the manuscript.

Chapter 2 contains the unpublished work: Kittur, H., et al. (2017). Probing cell adhesion profiles with a microscale adhesive choice assay. *Nature Methods* (sent for review). HK wrote the manuscript. HK, AT, AH, MY, and DD revised the manuscript.

Chapter 3 contains the work: Kittur, H., et al. (2014). Well-plate mechanical confinement platform for studies of mechanical mutagenesis. *Biomedical Microdevices*, 16: 439-447. HK wrote the manuscript. HK, WW, and DD revised the manuscript.

Harsha Kittur

Education

PhD in Bioengineering · UCLA — Expected March 2017

BS in Biological Systems Engineering · Virginia Tech · Summa Cum Laude — May 2011

Select Awards

Biological Systems Engineering Outstanding Recent Alumnus, Virginia Tech — March 2017

Biological Systems Engineering Outstanding Senior, Virginia Tech — May 2011

American Society of Agricultural and Biological Engineers Outstanding Junior, Virginia Tech — May 2010

Skills

Technical: surface chemistry · protein conjugation · immunocytochemistry · mammalian cell culture · photolithography · 3D printing · microfabrication · laser cutting · fluorescent and confocal microscopy · microfluidics

Computer: MATLAB · RStudio · ImageJ · AutoCAD · Inventor · COMSOL Multiphysics · Inkscape · Microsoft Office Suite

Research

Doctoral Researcher, Dino Di Carlo Lab, UCLA — Summer 2012 – Present

- Designed and built a patented diagnostic tool that tests cell transfer to new protein-coated surfaces, producing 64 new adhesion-based biomarkers to predict breast cancer metastasis, and resulting in 2 conference presentations in Singapore and Korea and 1 first author paper sent for review
- Mentored 2 high school students and 2 undergraduate researchers to design and construct a more user-friendly 3D printed system to increase experimental efficiency by 33 %
- Led our team of 20+ researchers to set up new laboratory spaces, maintain safety and cleanliness, and train others on equipment and protocols
- Built a tool to quantify abnormal asymmetric and multipolar divisions when cancer cells are mechanically compressed, culminating in 2 conference presentations and 1 first-author paper in *Biomedical Microdevices*

Leadership and Mentorship

Assistant Coordinator of the High School Summer Research Program, UCLA — Summer 2012 – Summer 2016

- Mentored 280 high school students to analyze scientific literature and to communicate their engineering research through oral presentations, poster presentations, and scientific reports, yielding 95 % satisfaction among students
- Wrote a first-author paper (sent for review) to showcase the program's teaching model and impact, which demonstrates a 4x increased admission rate for students applying to the UCLA School of Engineering

President of Engineering Graduate Student Association, UCLA — Fall 2015 – Spring 2016

- Led a team of 14 officers to plan and execute weekly professional development, social networking, and community outreach opportunities for 2000 engineering graduate students, and tripled student attendance

Teaching Associate for upper-division undergraduate classes (7 times), UCLA Fall 2011 – Spring 2013

- Taught biochemistry and bioengineering undergraduates technical lab skills: live/dead staining, BCA, MTS, 3D gel encapsulation, microcontact printing, replica molding, primer design, gene splicing, and protein purification

Patents

Kittur, H. and Di Carlo, D. (October 2015). Cell adhesion profiler and enrichment assay. US Patent 62/237,442.

Peer-Reviewed Original Publications

Kittur, H., et al. (2014). Well-plate mechanical confinement platform for studies of mechanical mutagenesis. *Biomedical Microdevices*, 16: 439-447.

Salmanzadeh, A., Kittur, H., Sano, M. B., Roberts, P. C., Schmelz, E. M., & Davalos, R. V. (2012). Dielectrophoretic differentiation of mouse ovarian surface epithelial cells, macrophages, and fibroblasts using contactless dielectrophoresis. *Biomicrofluidics*, *6*(2).

Review Publications

Koh, J., Wu, C.Y., Kittur, H., and Di Carlo, D. (2015). Research highlights: microfluidically-fabricated materials. *Lab on a Chip.* 15: 3818-3821.

Kunze, A., Pushkarsky, I., Kittur, H., and Di Carlo, D. (2014). Research highlights: measuring and manipulating cell migration. *Lab on a Chip.* 14: 1226-1229.

Weaver, W., Kittur, H., Dhar, M., and Di Carlo, D. (2014). Research highlights: microfluidic point-of-care diagnostics. *Lab on a Chip.* 14: 1962-1965.

Tseng, P., Kunze, A., Kittur, H., and Di Carlo, D. (2014). Research highlights: microtechnologies for engineering the cellular environment. *Lab on a Chip.* 14: 1226-1229.

Weaver, W., Tseng, P., Kunze, A., Masaeli, M., Chung, A., Dudani, J., Kittur, H., Kulkarni, R., Di Carlo, D. (2014). Advances in high-throughput single-cell microtechnologies. *Current Opinion in Biotechnology*, 25: 114-123.

Conference Presentations

Kittur, H., et al. (2016, October). Relative adhesion profiler system for biophysical interrogation of malignant breast cancer phenotypes. Poster presented at Biophysical Society Meeting: Mechanobiology of Disease. Singapore.

Kittur, H., et al. (2015, October). Multiplexed cell adhesion profiler system to characterize adhesive phenotypes of malignant cells. Paper presented at MicroTAS. Gyeongju, Korea.

Kittur H., et al. (2013, September). Massively parallel cell confinement platform for force balance studies. Poster presented at Biomedical Engineering Society. Seattle, WA.

Kittur H., et al. (2013 June). High-Throughput Tool for Cancer Proliferation Analysis Under Spatially Confined Conditions. UC Systemwide Bioengineering Symposium. San Diego, CA.

Chapter 1: Biophysical markers to supplement cancer prognosis

Cancer has been described for several millennia; however, a true understanding of the nature of the disease did not form until the last few centuries. In the 19th century, it was discovered that cancer is made up of cells that are derived from other cells, and that in addition to forming lesions, these cells can metastasize to other parts of the body that present habitable environments[1]. Also in the 19th century, after modern anesthesia was developed, surgeries became a widespread technique to remove tumors[2]. At the turn of the century, X-ray radiation was adopted for diagnosing and treating tumors[3,4].

Cancer screening techniques did not enter the medical field until the 20th century. In the 1920s, the Pap test was demonstrated as a method to identify cervical cancer[5], and became a widespread technique in the 1960s[6]. This was followed closely by the development and prevalent use of mammography for breast cancer screening. Alongside these methods, chemical and hormonal therapeutic agents were introduced to block or reduce tumor formation and spread, but at the risk of damaging healthy tissue.

The discovery of oncogenes and tumor-suppressor genes in the 1970s shed light on the complexities of cancer formation and the importance of genetic differences, leading to the rise of targeted therapies that interfere with specific molecules. The turn of this century has brought about next-generation sequencing techniques to rapidly study genomics and molecular biology in a cost-effective manner. This has greatly facilitated the discovery of numerous genetic biomarkers that can differentiate healthy cells from transformed tumor cells, and has sparked the development of corresponding diagnostic tools for early screening and treatment of cancer.

Due to the extensive heterogeneity of cancers, there is still a call to discover new biomarkers that complement existing ones, and to discover new screening strategies based off of those biomarkers. Mechanobiology is an emerging field that directly studies the physical forces that govern cell response in development, immune response, and disease. Typically, cells can be studied by (1) their inherent mechanical properties, (2) imposed mechanical forces from the environment, and (3) mechanical forces generated by the cell[7].

Discovery of new physical biomarkers relies on a deeper understanding of the changes in force balance and physical states of cells over time, as well as such changes in their unique microenvironments[8]. Observed physical changes can then be correlated with transcriptional, translational, and metabolic changes to develop a more holistic view of the disease. These properties can then be exploited in assays for characterizing and diagnosing disease state cells or for identifying rare subpopulations of cells with unique physical responses. As an added benefit, physical biomarkers can lead to methods of enriching such rare subpopulations that keep these cells intact, which could reduce noise in DNA and physical readouts from background cells. In this review, we will discuss popular physical biomarkers and how they are assayed, along with their applications.

1.1 Brief Overview of the Physical Requirements for Metastasis

According to the current model for metastasis, cancer cells undergo numerous physical changes in response to different physiological conditions that permit them to leave their original tumor and eventually colonize a new destination elsewhere in the body, as shown in figure 1[9]. Starting in the primary tumor, cells experience compressive forces from neighboring tumor cells as the tumor continues to grow. A sub-population of tumor cells undergo epithelial-to-

mesenchymal transition, which is characterized by a cascade of physiological changes, including the loss of E-cadherin expression on their surfaces, and thereby a loss in cell-cell adhesions[10]. This allows cells to thrive individually. From there, these cells can degrade their surrounding basement membrane to invade the collagen I rich stroma, where changes in adhesion are required to migrate. In conjunction with the release of degrading molecules, cells must be pliable enough to squeeze through the endothelial lining and enter the blood stream. Eventually, these circulating cells must adhere to the blood vessel wall and pass through it to invade and colonize the secondary tumor site.

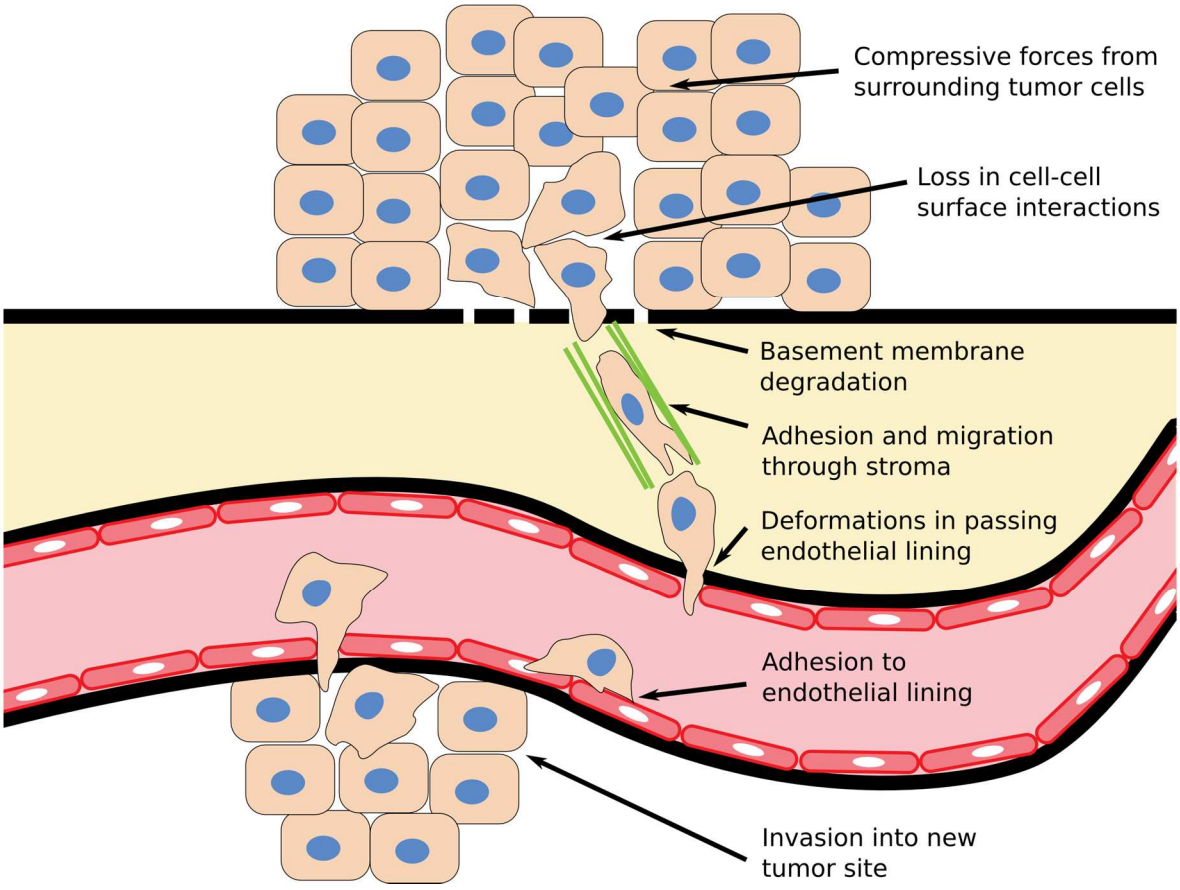

Figure 1: Cell-environment physical interactions involved in metastasis. Courtesy of Janay Kong.

Herein, we discuss cell size, deformability, adhesion, migration, and surface expression as key properties in cancer metastasis. Figure 2 shows the number of published articles to date for keyword searches in Web of Science following 'cancer' (e.g. 'cancer' AND 'adhesion' AND 'diagnostic'). For each property, we explore the biological relevance as well as its advantages and disadvantages in applications such as developing diagnostics, enriching cell subpopulations, and screening for anti-cancer drugs.

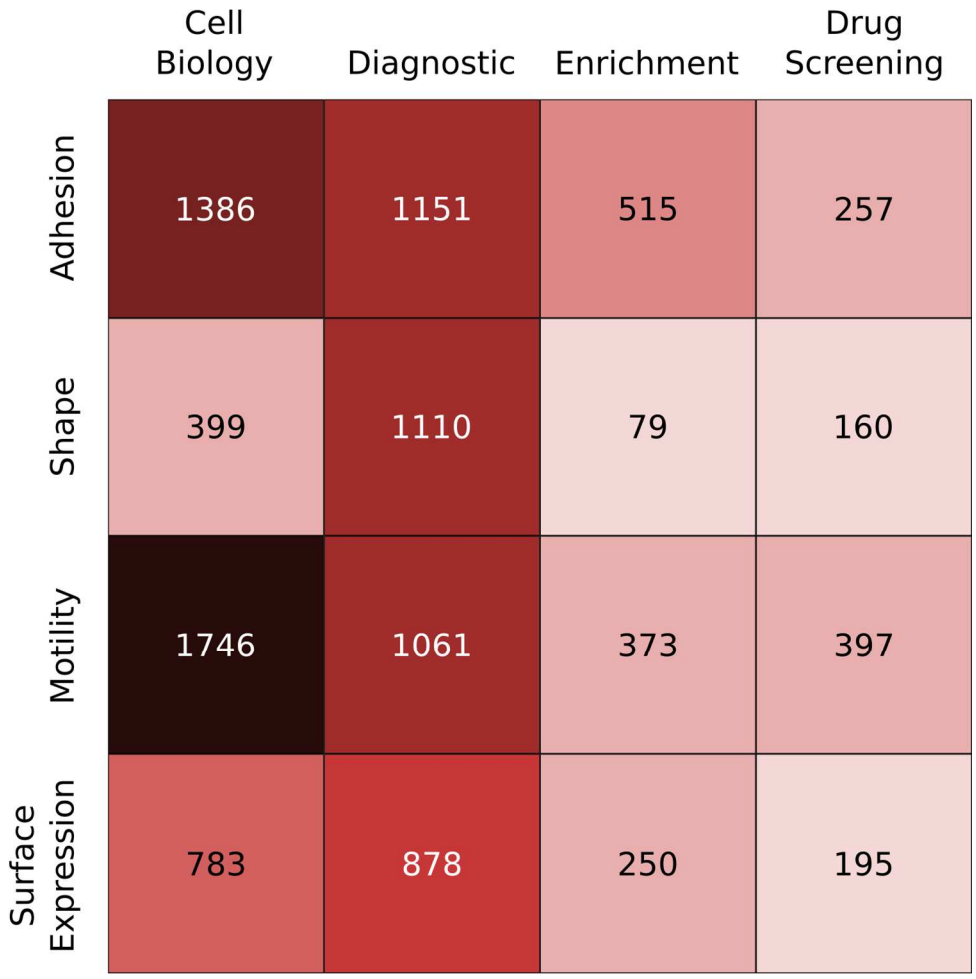

Figure 2: Web of Science publications for keyword searches in 'cancer' AND '[physical property]' AND '[application]'

1.2 Size and Deformability

Perhaps the clearest physical property of cells is their size. Differences in cell size are related to proliferation speed[11] and cell cycle[12]. Several gene regulators are closely related to cell growth. For example, Myc is frequently overexpressed in cancers, which can lead to increased cell size[13]. However, because size is so dependent on the anabolic and catabolic activity of cells that are regulated by numerous dynamic signaling pathways, it is difficult to correlate cell size to tumorigenicity.

A closely linked parameter, cell deformability, distinctly varies by tissue type and differentiation stage, where the stiffest cells are found in bone, less stiff cells in connective tissue, and softest cells in fat[14]. Cell stiffness is dependent on the interplay between the cytoskeleton and the nucleus, which is the largest organelle in the cell and can be 3-10 times stiffer, and nearly twice as viscoelastic as the cytoplasm[15,16]. Nuclear elasticity is a function of the chromatin packing and nuclear lamina composition[14].

A cell's ability to pass through narrow gaps will depend on the geometry and stiffness of both the cell and the surrounding matrix, along with the cell's ability to degrade and remodel the matrix. The nucleus can reduce its cross-sectional space down to 10 % to pass through pores[17]. In confined regions, cancer cells can adopt a faster amoeboid motility that is guided by pseudopodial protrusions and increase in actomyosin contractility[18]. *In vitro* tools have been used to show potential challenges that occur when exposed to high compressive forces, including nuclear rupture[19,20], and asymmetric and multipolar divisions for aneuploid cells with extra centrosomes[21–23]. Interestingly, for cells with supernumerary centrosomes it has been found that adhesion patterns in interphase can change the cell shape from polarized to rounded to induce a higher frequency of multipolar divisions[24].

Conversely, cell stretchers have been used to study strain-induced cytoskeletal fluidization, resolidification, reinforcement, and reorganization, as highlighted in other reviews on cell mechanics[25]. Cell stretchers and compressors can be low-cost, easy to use, and parallelized to many cells at once, but may be disadvantaged by anisotropy of applied force[25].

It is widely reported that mesenchymal cells tend to be more deformable than normal epithelial cells, and that deformability shares a positive correlation with metastatic potential[26–28]. Both cancer and normal cells are vastly less deformable than blood cells, so deformability can be a useful parameter for enrichment. However, due to the heterogeneity of CTCs, it is likely that some CTCs have biomechanical semblance to red blood cells[29].

Micropipette aspiration[30,31], characterized by pressure differential-based uptake of part of a cell's cytoplasm and nucleus, is widely used to for single-cell measurements of deformability, with particular advantage with non-adherent cells[32,33]. Though deformability measurements in this setting are highly correlated to size, discrepancies are at least partially reconciled with the power law fluid model[34].

Other deformability measurements are performed with optical and magnetic forces. Optical tweezers are popular for their sub-femtonewton resolution and non-contact force application[35]. Potential disadvantages include the necessity of aqueous solutions, limits in number of particles that can be trapped simultaneously, and photodamage with high intensity lasers[25]. In magnetic twisting cytometry, magnetic beads are bound to cell surface receptors, followed by magnetically-induced shear forces at a wide range of force (piconewtons to nanonewtons) and frequency (0-1000 Hz)[36]. This technique removes risk of photodamage and

limitations of the suspension medium, and provides a large range of different, and constant forces with versatility in bead attachment[25]. However, there are resolution limits, non-uniformity in the stress profile, and magnetic variability within the bead population[25].

Perhaps the most popular of these tools is atomic force microscopy (AFM), which uses a microscopic cantilever to indent cells, and records the corresponding force based off of cantilever displacement. AFM can be exceptionally precise and can measure time-dependent deformability through modulated frequencies of indentation.

It is known that cell stiffness is due, in part, to composition and organization of cytoskeletal components such as actin, microtubules, and intermediate filaments[37]. Indeed, AFM has been used to show that cancer cell elasticity may be due to reduced actin bundles in their apical regions as opposed to healthy cells[38], but also that cancer cells become much stiffer during invasion, pointing to actomyosin contractility as an important contributor[39]. Further, AFM has been applied to tumor biopsies to stage cancer progression by nanomechanical responses, and to show that tumor stiffness is greater at the periphery than at the core[40].

While all of these techniques provide useful biological information through precise deformability measurements at a single cell level with very minimal cell damage, more high-throughput techniques are needed for diagnostics. Perhaps the most biologically relevant *in vitro* method of measuring deformability is to look at invasion through narrow pores in microfluidic systems and measure residence time in those pores[29]. This tends to lump together many parameters at once, including cell size, deformability, and friction with the pore surface. Byun, et al. describe a method to decouple these parameters and find that less friction may promote cancer invasiveness[41].

Deformability cytometries test single cell deformation in a high-throughput manner (>100,000 cells). The hydrodynamic stretching approach deforms cells with two opposing microfluidic streams at a cross junction; the resulting cell deformation is captured with a high-speed camera[42]. This technique has been used to diagnose malignancy using pleural effusions[43]. Alternatively, hydrodynamic compression through sheath flow in a narrow channel has demonstrated real-time deformation measurements for cells in different cell cycle stages[44].

In optical stretching, cells are placed in between two opposing laser beams, which induce equal and opposite forces on the cell to stretch it[27]. This laser beam force is applied on the entire cell without direct contact, but cannot assay adherent cells[45]. Still, it has been useful in confirming that cancer cells tend to be more deformable than normal epithelial cells[46,47].

Size-based separation technologies are popular for isolating circulating tumor cells (CTCs) from blood as a diagnostic for cancer detection. For example, the typically larger and stiffer CTCs can be physically trapped in microfluidic filtration systems as blood flows through[48,49]. Filter clogging can be overcome with periodic mechanical disruption[50,51]. Other technologies avoid physical filters completely and can separate CTCs through negative depletion methods using inertial flows[52,53] or vorticies[54]. Inefficiencies may arise from heterogeneity in CTC size[55]. It is important to note that changes in cell size are disease-specific; small cell lung carcinomas tend to be smaller than normal cells and may be difficult to distinguish from blood.

Dielectrophoresis (DEP), characterized by the polarization and motion of neutrally charged particles in non-uniform fields, is given as a force that is dependent on the permittivity of the surrounding medium, the polarizability of the particle, the size of the particle, and the amplitude and frequency of the electric field[56]. While intrinsic macromolecules do impact the dielectric properties of a cell, Cell size plays a large role since $F_{DEP} \sim r^3$ [56], but intrinsic

macromolecules on the surface and in the cytoplasm do impact the dielectric properties. DEP force has been used to separate live and dead cells[57] as well as cancer cells from blood due to their differential response in non-uniform electric fields[58]. Non-uniform electric fields, sometimes in combination with previously mentioned hydrodynamic techniques, have been used to enrich breast[59,60] or ovarian cancer cells[61]. DEP is label-free, and various techniques[62] are being explored to address the common challenge of cell damage by Joule heating and bubble formation.

Acoustophoresis in microchannels allows cells to be separated by ultrasonic standing waves with little impact from the ionic properties of the media. While compressibility and density play a role, acoustophoretic force induced on a cell is strongly linked to cell size ($F_A \sim r^3$), so it is ideal for separating live and dead cells[63], cancer cells from blood[64], and leukocyte subpopulations (lymphocytes, monocytes, and granulocytes)[65]. Still acoustic forces have be used to confirm that more metastatic cells are more compressible[66].

Differences in deformability can lead to enrichment tools that can isolate rare subpopulations of cells for downstream analysis. In microfluidic systems, inertial flows can apply viscoelastic force on a train of cells entering an expansion region, and the differential lift forces can separate cells by their deformability[54].

1.3 Adhesion

Cancer progression is characterized by numerous changes in adhesive and degradation mechanisms that allow cells to remodel and thrive in new environments. Pre-metastatic tumor cells can undergo epithelial-mesenchymal transition (EMT), a cascade of alterations in which

cells replace their epithelial cell polarity and cell-cell interactions, in favor of a motile and invasive phenotype. After this transition, they express MMPs on their surface. This allows them to degrade components of the basement membrane[67], including laminin and collagen IV, which gives them access to leave the tumor microenvironment and seek new environments that are more rich in collagen 1 and fibronectin. Fibroblasts in this region release lysyl oxidase, which cross-link collagen and fibronectin, enhancing integrin signaling and promoting cell adhesion and migration.

Adhesive force in cell-ECM interactions is often tested by measuring the force required to break the interaction. AFM tips that are functionalized with specific adhesion molecules have been used to precisely quantify single cell adhesion strength to that type of molecule[68,69]. Micropipette aspiration can apply a controllable detachment force to adherent cells, and has been used to show that detachment force scales with spread area[70].

In scaling up to larger sample sizes, the simplest detachment approach is the plate-and-wash assay, which can give some information about specificity to adhesion receptors and the initial rate of adhesions, but cannot provide enough shear force to detach fully adherent cells[71]. Spinning disc assays, which apply enough shear stress to detach adhered cells, give measurements that are more indicative to the number of adhesive bonds rather than initial rate of adhesion[71,72]. They have been used to demonstrate that myosin II tenses the actin filaments to switch integrins from a relaxed state to an active state[73], increasing binding strength.

Studies have shown that ECM concentration positively correlates with cell adhesion strength[74], and that tuning the surface properties around the ECM can change a cell's behavior from attractive to repulsive from the ECM[75]. More complex ECM formulations and substrate

stiffnesses that mimic specific organs have been used to fingerprint breast cancer cell types by observation of several morphological parameters[76].

Most of these adhesive assays look at cell spreading on 2D ECM-coated surfaces. While differential cell spreading patterns on 2D surfaces may distinguish cell types, and are appropriate for modeling adhesion to blood vessels, they do not resemble the 3D cell behavior in most physiological microenvironments. For example, on 2D surfaces, cells are found to polarize and produce focal adhesions, temporary actin-rich structures that anchor cells to the surface during migration. However, in 3D environments, cells do not form focal adhesions and have fewer stress fibers[77].

For this reason, studies are moving beyond 2D environments. Guzman, et al. have cells envelope themselves into 3D basement membrane spheroids that are embedded in collagen I gels to observe degradation and invasion[78]. Additionally, breast cancer cells have been characterized by their ability to switch from one ECM-coated surface to another in a multiplexed format [see Chapter 3].

Hydrodynamic shear in microchannels can be used to test the adhesion strength of cells bound to specific protein-coated surfaces[74], and can even be used to separate subpopulations that are more weakly adhered[79]. Because adhesion is not limited to the interaction with ECM proteins; properties like geometry[80] and nanotopology[81,82] can be tuned in microdevices for characterization and separation.

One caveat is that fluidic forces can affect cell adhesion and spreading, and play an essential role in tumorigenesis. In some cancers, such as esophageal cancer, shear stresses may coax cells to internalize E-cadherin from their surface, thereby promoting invasiveness[83]. In

other cases, interstitial flow primes fibroblasts to remodel the local environment[84], which can pave the way for tumor cells to invade and intravasate. Blood flow carries these cells to their eventual destination, where they may extravasate and colonize the secondary site[77]. Venous shear stresses were shown to stimulate actomyosin contraction, which results in dynamic bleb-based invasion and adhesion in metastatic esophogial cancer cells[85]. Therefore, it is important to ensure that hydrodynamic shear-based separation systems do not change cell properties.

Adhesion is not limited to ECM proteins. Smaller peptide sequences like RGD are found in several ECM proteins and can similarly coax cell attachment, while having the additional advantages of precise synthetic production and resistance to pH and heat denaturation[86]. Systematic Evolution of Ligands by Exponential Enrichment (SELEX) is a technique used to discover nucleic acid aptamers that bind to targets with similar selectivity to that of antibodies, but have the additional advantage of low cost due to the capability to be amplified through PCR. Aptamers have been used to enrich and detect different rare cancers in microfluidic systems[87]. While these molecules may not match the physiological relevance of ECM proteins, they offer simplicity or selectivity that may be very useful for precise detection and isolation of rare populations for downstream analysis[88].

1.4 Migration

The degree to which cells degrade, remodel, and adhere to different environments may be cell-specific, and can therefore also determine the cell's motility. This can be compounded by growth factors that influence motogenic activity[89]. Due to the long time scale for cell migration, it is not a typical or scalable parameter that can be applied to a diagnostic or enrichment

technology. For this reason, cell migration is heavily studied as a means of understanding basic cancer biology or screening for drugs.

The scratch wound assay, which scratches a confluent monolayer of cells on a 2D surface and monitors their proliferation, cell-cell interactions, cell-ECM adhesions, and migration to close the initial "wound"[90], is popular for motility studies and has been expanded to high throughput screening in 384-well plates[91]. One limitation is that the scratch damages the cells and ECM in that region. Sometimes a barrier assay is used instead, where the gap is created by lifting a barrier after confluency[92].

Several transmembrane assays were designed to study cell migration in response to a chemical stimulus. The most popular of these is the Boyden chamber assay. Developed in 1962, this technique tests cell transmigration from a control environment to a test substance across a filter[93], and has been used to study growth factor[94] or chemokine[95] mediated cancer migration cancer drug screening[96]. Some of the drawbacks of transmembrane assays are that they can be technically challenging to use, and include a non-linear chemical gradient that equilibrates with both compartments over time[97].

Finally, microfluidic devices have been designed to study cancer invasion in 3D matricies[98,99]. These devices use less reagents, which is particularly useful when working with rare or primary cells where numbers are limited[100].

Furthermore, cancer cells are not restricted to single cell migration, mediated by integrin-ECM adhesion. Cell-cell adhesions are present in cancer cells that invade through 3D environments in clusters[101,102]. These clusters can become polarized such that "pioneer" cells lead their cell cohorts of "followers"[103]. Several tools have been developed to study collective

cell migration, including ECM-coated pillar arrays microfluidic channels[102] and epithelial bridges[104].

1.5 Surface expression

Surface proteins are another popular source for physical biomarkers, as each cell has its own unique landscape. Epithelial cells tend to express high levels of E-cadherin, while cells that have undergone epithelial-to-mesenchymal transition (EMT) express high levels of vimentin. Epithelial cell adhesion molecule (EpCAM) is frequently overexpressed in several cancers[105].

Therefore, anti-EpCAM is widely used in microdevices to enrich CTCs[106], with high capture efficiency. However, purity tends to be low, and some CTCs might be lost due to heterogeneity due to low EpCAM expression after EMT[107]. DEP forces may be used to attract CTCs with low EpCAM expression so that they may be captured with immobilized antibodies, while simultaneously repelling blood cells from the vicinity[107]. Other surface markers, such as epithelial membrane antigen (EMA) and epithelial growth factor receptor (EGFR), have been explored for breast cancer capture in microfluidic systems[108].

Fluorescence activated cell sorting (FACS) is the current gold standard separation technique. Cells differentially expressing a given surface marker(s) are fluorescently tagged and are forced into a train of cells. Each cell's fluorescent signature is identified with a laser and subsequently deflected and sorted downstream. While this is a reliable method of sorting cells, it requires expensive reagents and technical skill. Additionally, it is not label-free, so cells may not be recovered for further analysis.

A similar technique, magnetic activated cell sorting (MACS) tags surface markers with magnetic nanoparticles instead of fluorescently labeled antibodies. Typically a magnet suspends

the tagged cells while all other cells are eluted through negative depletion[109]. 1000-fold depletion rates for more than 10^9 cells can be achieved in 15 minutes[109]. While FACS can quantify level of surface marker expression, MACS is typically limited to binary quantification. However, MACS has been extended to labeling cells with multiple targets[110], or more recently a magnetic ratcheting system to segregate cells by degree of magnetic labeling[111].

The Miltenyi MACs system is a commercially available magnetic-based cell sorter and has been shown to separate cytokeratin (CK) positive breast cancer cells from blood[112]. It has also been used to label and separate breast cancer cells by their expression of CXCR4, a chemokine receptor that is upregulated in bone marrow-metastasizing cells[113]. CellSearch, the only FDA-approved CTC detection system on the market, relies on staining and magnetic labeling of surface markers CD45, CK[114]. Efficiency is limited by the heterogeneity in surface marker expression levels like EpCAM, especially if the CTCs have undergone EMT[115], which results in reduced expression of epithelial markers.

1.6 Conclusion

Here we have discussed the importance for phenotypic markers in understanding cancer biology, and using that knowledge to develop new tools for cancer prognosis. Yet, new tools must continue to assay novel biomarkers to shed more light into the aberrant and heterogeneous phenotypes of different cancers. The next few chapters discuss the development of new in vitro platforms that enable analyses of cell behavior and intermolecular processes in specific microenvironments.

1.7 References

1. Paget, S. The distribution of secondary growths in cancer of the breast. *The Lancet* **133,** 571–573 (1889).
2. Greene, N. M. Anesthesia and the development of surgery (1846-1896). *Anesth. Analg.* **58,** 5–12 (1979).
3. Baskar, R., Lee, K. A., Yeo, R. & Yeoh, K.-W. Cancer and Radiation Therapy: Current Advances and Future Directions. *Int. J. Med. Sci.* **9,** 193–199 (2012).
4. Röntgen, W. C. On a New Kind of Rays. *Science* **3,** 227–231 (1896).
5. Marinakis, Y., Marinaki, M. & Dounias, G. Particle swarm optimization for pap-smear diagnosis. *Expert Syst. Appl.* **35,** 1645–1656 (2008).
6. Safaeian, M. & Solomon, D. Cervical Cancer Prevention - Cervical Screening: Science in Evolution. *Obstet. Gynecol. Clin. North Am.* **34,** 739–ix (2007).
7. Reinhart-King, C. A. in *Physical Sciences and Engineering Advances in Life Sciences and Oncology* (eds. Janmey, P. et al.) 49–71 (Springer International Publishing, 2016).
8. Darling, E. M. & Di Carlo, D. High-Throughput Assessment of Cellular Mechanical Properties. *Annu. Rev. Biomed. Eng.* **17,** 35–62 (2015).
9. Bacac, M. & Stamenkovic, I. Metastatic Cancer Cell. *Annu. Rev. Pathol. Mech. Dis.* **3,** 221–247 (2008).
10. Kalluri, R. & Weinberg, R. A. The basics of epithelial-mesenchymal transition. *J. Clin. Invest.* **119,** 1420–1428 (2009).
11. Rouzaire-Dubois, B., Malo, M., Milandri, J.-B. & Dubois, J.-M. Cell size-proliferation relationship in rat glioma cells. *Glia* **45,** 249–257 (2004).
12. Son, S. *et al.* Direct observation of mammalian cell growth and size regulation. *Nat. Methods* **9,** 910–912 (2012).
13. Li, Q., Rycaj, K., Chen, X. & Tang, D. G. Cancer stem cells and cell size: A causal link? *Semin. Cancer Biol.* **35,** 191–199 (2015).

14. Krause, M. & Wolf, K. Cancer cell migration in 3D tissue: Negotiating space by proteolysis and nuclear deformability. *Cell Adhes. Migr.* **9,** 357–366 (2015).
15. Guilak, F., Tedrow, J. R. & Burgkart, R. Viscoelastic Properties of the Cell Nucleus. *Biochem. Biophys. Res. Commun.* **269,** 781–786 (2000).
16. Caille, N., Thoumine, O., Tardy, Y. & Meister, J.-J. Contribution of the nucleus to the mechanical properties of endothelial cells. *J. Biomech.* **35,** 177–187 (2002).
17. Wolf, K. *et al.* Physical limits of cell migration: Control by ECM space and nuclear deformation and tuning by proteolysis and traction force. *J Cell Biol* **201,** 1069–1084 (2013).
18. Liu, Y.-J. *et al.* Confinement and low adhesion induce fast amoeboid migration of slow mesenchymal cells. *Cell* **160,** 659–672 (2015).
19. Denais, C. M. *et al.* Nuclear envelope rupture and repair during cancer cell migration. *Science* **352,** 353–358 (2016).
20. Le Berre, M., Aubertin, J. & Piel, M. Fine control of nuclear confinement identifies a threshold deformation leading to lamina rupture and induction of specific genes. *Integr. Biol.* **4,** 1406 (2012).
21. Kittur, H., Weaver, W. & Di Carlo, D. Well-plate mechanical confinement platform for studies of mechanical mutagenesis. *Biomed. Microdevices* **16,** 439–447 (2014).
22. Tse, H. T. K., Weaver, W. M. & Di Carlo, D. Increased Asymmetric and Multi-Daughter Cell Division in Mechanically Confined Microenvironments. *PLoS ONE* **7,** e38986 (2012).
23. Lancaster, O. M. *et al.* Mitotic Rounding Alters Cell Geometry to Ensure Efficient Bipolar Spindle Formation. *Dev. Cell* **25,** 270–283 (2013).
24. Kwon, M. *et al.* Mechanisms to suppress multipolar divisions in cancer cells with extra centrosomes. *Genes Dev.* **22,** 2189–2203 (2008).
25. Rodriguez, M. L., McGarry, P. J. & Sniadecki, N. J. Review on Cell Mechanics: Experimental and Modeling Approaches. *Appl. Mech. Rev.* **65,** 060801-060801-41 (2013).
26. Xu, W. *et al.* Cell stiffness is a biomarker of the metastatic potential of ovarian cancer cells. *PloS One* **7,** e46609 (2012).

27. Guck, J. *et al.* Optical deformability as an inherent cell marker for testing malignant transformation and metastatic competence. *Biophys. J.* **88,** 3689–3698 (2005).
28. Swaminathan, V. *et al.* Mechanical Stiffness Grades Metastatic Potential in Patient Tumor Cells and in Cancer Cell Lines. *Cancer Res.* **71,** 5075–5080 (2011).
29. Bagnall, J. S. *et al.* Deformability of Tumor Cells versus Blood Cells. *Sci. Rep.* **5,** 18542 (2015).
30. Lee, L. M., Lee, J. W., Chase, D., Gebrezgiabhier, D. & Liu, A. P. Development of an advanced microfluidic micropipette aspiration device for single cell mechanics studies. *Biomicrofluidics* **10,** 054105 (2016).
31. Shojaei-Baghini, E., Zheng, Y. & Sun, Y. Automated Micropipette Aspiration of Single Cells. *Ann. Biomed. Eng.* **41,** 1208–1216 (2013).
32. Tsai, M. A., Waugh, R. E. & Keng, P. C. Cell cycle-dependence of HL-60 cell deformability. *Biophys. J.* **70,** 2023–2029 (1996).
33. Tran-Son-Tay, R., Needham, D., Yeung, A. & Hochmuth, R. M. Time-dependent recovery of passive neutrophils after large deformation. *Biophys. J.* **60,** 856–866 (1991).
34. Tsai, M. A., Frank, R. S. & Waugh, R. E. Passive mechanical behavior of human neutrophils: power-law fluid. *Biophys. J.* **65,** 2078–2088 (1993).
35. Zhang, H. & Liu, K.-K. Optical tweezers for single cells. *J. R. Soc. Interface* **5,** 671–690 (2008).
36. Wang, Y.-L. & Discher, D. E. *Cell Mechanics*. (Academic Press, 2007).
37. Suresh, S. *et al.* Connections between single-cell biomechanics and human disease states: gastrointestinal cancer and malaria. *Acta Biomater.* **1,** 15–30 (2005).
38. Calzado-Martín, A., Encinar, M., Tamayo, J., Calleja, M. & San Paulo, A. Effect of Actin Organization on the Stiffness of Living Breast Cancer Cells Revealed by Peak-Force Modulation Atomic Force Microscopy. *ACS Nano* **10,** 3365–3374 (2016).
39. Staunton, J. R., Doss, B. L., Lindsay, S. & Ros, R. Correlating confocal microscopy and atomic force indentation reveals metastatic cancer cells stiffen during invasion into collagen I matrices. *Sci. Rep.* **6,** 19686 (2016).

40. Plodinec, M. *et al.* The nanomechanical signature of breast cancer. *Nat. Nanotechnol.* **7,** 757–765 (2012).
41. Byun, S. *et al.* Characterizing deformability and surface friction of cancer cells. *Proc. Natl. Acad. Sci.* **110,** 7580–7585 (2013).
42. Gossett, D. R. *et al.* Hydrodynamic stretching of single cells for large population mechanical phenotyping. *Proc. Natl. Acad. Sci.* **109,** 7630–7635 (2012).
43. Tse, H. T. K. *et al.* Quantitative Diagnosis of Malignant Pleural Effusions by Single-Cell Mechanophenotyping. *Sci. Transl. Med.* **5,** 212ra163-212ra163 (2013).
44. Otto, O. *et al.* Real-time deformability cytometry: on-the-fly cell mechanical phenotyping. *Nat. Methods* **12,** 199–202 (2015).
45. Lee, G. Y. H. & Lim, C. T. Biomechanics approaches to studying human diseases. *Trends Biotechnol.* **25,** 111–118 (2007).
46. Lincoln, B. *et al.* Deformability-based flow cytometry. *Cytometry A* **59,** 203–209 (2004).
47. Wottawah, F. *et al.* Characterizing single suspended cells by optorheology. *Acta Biomater.* **1,** 263–271 (2005).
48. Tan, S. J. *et al.* Versatile label free biochip for the detection of circulating tumor cells from peripheral blood in cancer patients. *Biosens. Bioelectron.* **26,** 1701–1705 (2010).
49. Hvichia, G. e. *et al.* A novel microfluidic platform for size and deformability based separation and the subsequent molecular characterization of viable circulating tumor cells. *Int. J. Cancer* **138,** 2894–2904 (2016).
50. Qin, X. *et al.* Size and deformability based separation of circulating tumor cells from castrate resistant prostate cancer patients using resettable cell traps. *Lab Chip* **15,** 2278–2286 (2015).
51. Yoon, Y. *et al.* Clogging-free microfluidics for continuous size-based separation of microparticles. *Sci. Rep.* **6,** 26531 (2016).
52. Hou, H. W. *et al.* Isolation and retrieval of circulating tumor cells using centrifugal forces. *Sci. Rep.* **3,** (2013).

53. Claire Hur, S., K. Henderson-MacLennan, N., B. McCabe, E. R. & Carlo, D. D. Deformability-based cell classification and enrichment using inertial microfluidics. *Lab. Chip* **11,** 912–920 (2011).
54. Hur, S. C., Mach, A. J. & Carlo, D. D. High-throughput size-based rare cell enrichment using microscale vortices. *Biomicrofluidics* **5,** 022206 (2011).
55. Chen, X.-X. & Bai, F. Single-cell analyses of circulating tumor cells. *Cancer Biol. Med.* **12,** 184–192 (2015).
56. Pethig, R. Review Article—Dielectrophoresis: Status of the theory, technology, and applications. *Biomicrofluidics* **4,** 022811 (2010).
57. Jen, C.-P. & Chen, T.-W. Selective trapping of live and dead mammalian cells using insulator-based dielectrophoresis within open-top microstructures. *Biomed. Microdevices* **11,** 597 (2009).
58. Becker, F. F. *et al.* Separation of human breast cancer cells from blood by differential dielectric affinity. *Proc. Natl. Acad. Sci.* **92,** 860–864 (1995).
59. An, J., Lee, J., Lee, S. H., Park, J. & Kim, B. Separation of malignant human breast cancer epithelial cells from healthy epithelial cells using an advanced dielectrophoresis-activated cell sorter (DACS). *Anal. Bioanal. Chem.* **394,** 801–809 (2009).
60. Moon, H.-S. *et al.* Continuous separation of breast cancer cells from blood samples using multi-orifice flow fractionation (MOFF) and dielectrophoresis (DEP). *Lab. Chip* **11,** 1118 (2011).
61. Salmanzadeh, A. *et al.* Dielectrophoretic differentiation of mouse ovarian surface epithelial cells, macrophages, and fibroblasts using contactless dielectrophoresis. *Biomicrofluidics* **6,** 024104 (2012).
62. Shafiee, H., Sano, M. B., Henslee, E. A., Caldwell, J. L. & Davalos, R. V. Selective isolation of live/dead cells using contactless dielectrophoresis (cDEP). *Lab. Chip* **10,** 438 (2010).
63. Yang, A. H. J. & Soh, H. T. Acoustophoretic Sorting of Viable Mammalian Cells in a Microfluidic Device. *Anal. Chem.* **84,** 10756–10762 (2012).
64. Augustsson, P., Magnusson, C., Nordin, M., Lilja, H. & Laurell, T. Microfluidic, Label-Free Enrichment of Prostate Cancer Cells in Blood Based on Acoustophoresis. *Anal. Chem.* **84,** 7954–7962 (2012).

65. Grenvall, C., Magnusson, C., Lilja, H. & Laurell, T. Concurrent Isolation of Lymphocytes and Granulocytes Using Prefocused Free Flow Acoustophoresis. *Anal. Chem.* **87,** 5596–5604 (2015).
66. Wang, H. *et al.* Acoustophoretic force-based compressibility measurement of cancer cells having different metastatic potential. in 045019–045019 (2013). doi:10.1121/1.4799801
67. Hotary, K., Li, X.-Y., Allen, E., Stevens, S. L. & Weiss, S. J. A cancer cell metalloprotease triad regulates the basement membrane transmigration program. *Genes Dev.* **20,** 2673–2686 (2006).
68. Cigne, A. L. *et al.* Analysis of the effect of LRP-1 silencing on the invasive potential of cancer cells by nanomechanical probing and adhesion force measurements using atomic force microscopy. *Nanoscale* **8,** 7144–7154 (2016).
69. Sen, S., Subramanian, S. & Discher, D. E. Indentation and Adhesive Probing of a Cell Membrane with AFM: Theoretical Model and Experiments. *Biophys. J.* **89,** 3203–3213 (2005).
70. Hogan, B., Babataheri, A., Hwang, Y., Barakat, A. I. & Husson, J. Characterizing Cell Adhesion by Using Micropipette Aspiration. *Biophys. J.* **109,** 209–219 (2015).
71. Boettiger, D. in (ed. Enzymology, B.-M. in) **426,** 1–25 (Academic Press, 2007).
72. Engler, A. J., Chan, M., Boettiger, D. & Schwarzbauer, J. E. A novel mode of cell detachment from fibrillar fibronectin matrix under shear. *J. Cell Sci.* **122,** 1647–1653 (2009).
73. Friedland, J. C., Lee, M. H. & Boettiger, D. Mechanically Activated Integrin Switch Controls α5β1 Function. *Science* **323,** 642–644 (2009).
74. Lu, H. *et al.* Microfluidic Shear Devices for Quantitative Analysis of Cell Adhesion. *Anal. Chem.* **76,** 5257–5264 (2004).
75. Ricoult, S. G., Thompson-Steckel, G., Correia, J. P., Kennedy, T. E. & Juncker, D. Tuning cell–surface affinity to direct cell specific responses to patterned proteins. *Biomaterials* **35,** 727–736 (2014).
76. Barney, L. E. *et al.* A cell–ECM screening method to predict breast cancer metastasis. *Integr. Biol.* **7,** 198–212 (2015).
77. Wirtz, D., Konstantopoulos, K. & Searson, P. C. The physics of cancer: the role of physical interactions and mechanical forces in metastasis. *Nat. Rev. Cancer* **11,** 512–522 (2011).

78. A novel 3D in vitro metastasis model elucidates differential invasive strategies during and after breaching basement membrane. Available at: http://www.sciencedirect.com/science/article/pii/S0142961216306226. (Accessed: 5th January 2017)
79. Singh, A. *et al.* Adhesion strength-based, label-free isolation of human pluripotent stem cells. *Nat. Methods* **10,** 438–444 (2013).
80. V. Green, J. *et al.* Effect of channel geometry on cell adhesion in microfluidic devices. *Lab. Chip* **9,** 677–685 (2009).
81. Kwon, K. W. *et al.* Label-free, microfluidic separation and enrichment of human breast cancer cells by adhesion difference. *Lab. Chip* **7,** 1461 (2007).
82. Westcott, N. P., Lamb, B. M. & Yousaf, M. N. Electrochemical and Chemical Microfluidic Gold Etching to Generate Patterned and Gradient Substrates for Cell Adhesion and Cell Migration. *Anal. Chem.* **81,** 3297–3303 (2009).
83. Lawler, K., O'Sullivan, G., Long, A. & Kenny, D. Shear stress induces internalization of E-cadherin and invasiveness in metastatic oesophageal cancer cells by a Src-dependent pathway. *Cancer Sci.* **100,** 1082–1087 (2009).
84. Shieh, A. C., Rozansky, H. A., Hinz, B. & Swartz, M. A. Tumor Cell Invasion Is Promoted by Interstitial Flow-Induced Matrix Priming by Stromal Fibroblasts. *Cancer Res.* **71,** 790–800 (2011).
85. Lawler, K., Foran, E., O'Sullivan, G., Long, A. & Kenny, D. Mobility and invasiveness of metastatic esophageal cancer are potentiated by shear stress in a ROCK- and Ras-dependent manner. *Am. J. Physiol. - Cell Physiol.* **291,** C668–C677 (2006).
86. LeBaron, R. G. & Athanasiou, K. A. Extracellular Matrix Cell Adhesion Peptides: Functional Applications in Orthopedic Materials. *Tissue Eng.* **6,** 85–103 (2000).
87. Xu, Y. *et al.* Aptamer-Based Microfluidic Device for Enrichment, Sorting, and Detection of Multiple Cancer Cells. *Anal. Chem.* **81,** 7436–7442 (2009).

88. Fatanat Didar, T. & Tabrizian, M. Adhesion based detection, sorting and enrichment of cells in microfluidic Lab-on-Chip devices. *Lab. Chip* **10,** 3043–3053 (2010).
89. Lampugnani, M. in *Adhesion Protein Protocols* (eds. Dejana, E. & Corada, M.) 177–182 (Humana Press, 1999). doi:10.1385/1-59259-258-9:177
90. Liang, C.-C., Park, A. Y. & Guan, J.-L. In vitro scratch assay: a convenient and inexpensive method for analysis of cell migration in vitro. *Nat. Protoc.* **2,** 329–333 (2007).
91. Yarrow, J. C., Perlman, Z. E., Westwood, N. J. & Mitchison, T. J. A high-throughput cell migration assay using scratch wound healing, a comparison of image-based readout methods. *BMC Biotechnol.* **4,** 21 (2004).
92. van Horssen, R. & ten Hagen, T. L. M. Crossing barriers: The new dimension of 2D cell migration assays. *J. Cell. Physiol.* **226,** 288–290 (2011).
93. Boyden, S. The Chemotactic Effect of Mixtures of Antibody and Antigen on Polymorphonuclear Leucocytes. *J. Exp. Med.* **115,** 453–466 (1962).
94. Saadi, W., Wang, S.-J., Lin, F. & Jeon, N. L. A parallel-gradient microfluidic chamber for quantitative analysis of breast cancer cell chemotaxis. *Biomed. Microdevices* **8,** 109–118 (2006).
95. Chen, J. *et al.* CCL18 from Tumor-Associated Macrophages Promotes Breast Cancer Metastasis via PITPNM3. *Cancer Cell* **19,** 541–555 (2011).
96. Kopp, F. *et al.* Salinomycin treatment reduces metastatic tumor burden by hampering cancer cell migration. *Mol. Cancer* **13,** 16 (2014).
97. Hulkower, K. I. & Herber, R. L. Cell Migration and Invasion Assays as Tools for Drug Discovery. *Pharmaceutics* **3,** 107–124 (2011).
98. Liu, T. *et al.* A microfluidic device for characterizing the invasion of cancer cells in 3-D matrix. *ELECTROPHORESIS* **30,** 4285–4291 (2009).
99. Liu, T., Lin, B. & Qin, J. Carcinoma-associated fibroblasts promoted tumor spheroid invasion on a microfluidic 3D co-culture device. *Lab. Chip* **10,** 1671–1677 (2010).

100. Echeverria, V. *et al.* An Automated High-Content Assay for Tumor Cell Migration through 3-Dimensional Matrices. *J. Biomol. Screen.* **15,** 1144–1151 (2010).

101. Friedl, P. *et al.* Migration of coordinated cell clusters in mesenchymal and epithelial cancer explants in vitro. *Cancer Res.* **55,** 4557–4560 (1995).

102. Wong, I. Y. *et al.* Collective and individual migration following the epithelial–mesenchymal transition. *Nat. Mater.* **13,** 1063–1071 (2014).

103. Friedl, P. & Gilmour, D. Collective cell migration in morphogenesis, regeneration and cancer. *Nat. Rev. Mol. Cell Biol.* **10,** 445–457 (2009).

104. Vedula, S. R. K. *et al.* Epithelial bridges maintain tissue integrity during collective cell migration. *Nat. Mater.* **13,** 87–96 (2014).

105. Went, P. T. H. *et al.* Frequent EpCam protein expression in human carcinomas. *Hum. Pathol.* **35,** 122–128 (2004).

106. Nagrath, S. *et al.* Isolation of rare circulating tumour cells in cancer patients by microchip technology. *Nature* **450,** 1235–1239 (2007).

107. Huang, C., Smith, J. P., Saha, T. N., Rhim, A. D. & Kirby, B. J. Characterization of microfluidic shear-dependent epithelial cell adhesion molecule immunocapture and enrichment of pancreatic cancer cells from blood cells with dielectrophoresis. *Biomicrofluidics* **8,** 044107 (2014).

108. Du, Z., Cheng, K. H., Vaughn, M. W., Collie, N. L. & Gollahon, L. S. Recognition and capture of breast cancer cells using an antibody-based platform in a microelectromechanical systems device. *Biomed. Microdevices* **9,** 35–42 (2007).

109. Miltenyi, S., Müller, W., Weichel, W. & Radbruch, A. High gradient magnetic cell separation with MACS. *Cytometry* **11,** 231–238 (1990).

110. Adams, J. D., Kim, U. & Soh, H. T. Multitarget magnetic activated cell sorter. *Proc. Natl. Acad. Sci.* **105,** 18165–18170 (2008).

111. Murray, C. *et al.* Quantitative Magnetic Separation of Particles and Cells Using Gradient Magnetic Ratcheting. *Small* **12,** 1891–1899 (2016).

112. Witzig, T. E. *et al.* Detection of Circulating Cytokeratin-positive Cells in the Blood of Breast Cancer Patients Using Immunomagnetic Enrichment and Digital Microscopy. *Clin. Cancer Res.* **8,** 1085–1091 (2002).

113. Cabioglu, N. *et al.* Chemokine receptor CXCR4 expression in breast cancer as a potential predictive marker of isolated tumor cells in bone marrow. *Clin. Exp. Metastasis* **22,** 39–46 (2005).

114. Miller, M. C., Doyle, G. V. & Terstappen, L. W. M. M. Significance of Circulating Tumor Cells Detected by the CellSearch System in Patients with Metastatic Breast Colorectal and Prostate Cancer. *J. Oncol.* **2010,** e617421 (2009).

115. Shim, S., Stemke-Hale, K., Noshari, J., Becker, F. F. & Gascoyne, P. R. C. Dielectrophoresis has broad applicability to marker-free isolation of tumor cells from blood by microfluidic systems. *Biomicrofluidics* **7,** 011808 (2013).

Chapter 2: Well-plate mechanical confinement platform for studies of mechanical mutagenesis

In this chapter, we discuss the impact of confined spaces on aneuploid cells during mitosis. Limited space for cell division, perhaps similar to the compressed microenvironment of a growing tumor, has been shown to induce phenotypic and karyotypic changes to a cell during mitosis. To expand understanding of this missegregation of chromosomes in aberrant multi-daughter or asymmetric cell divisions, we present a simple technique for subjecting mammalian cells to adjustable levels of confinement which allows subsequent interrogation of intracellular molecular components using high resolution confocal imaging. PDMS micropatterned confinement structures of subcellular height with neighboring taller media reservoir channels were secured on top of confluent cells by compression with a modified compression well-plate system. The system improved ease of use over previous devices since confined cells could be initially grown on glass coverslips in a 12-well plate, and subsequently be imaged by high resolution confocal imaging, or during compression by live cell imaging. Live cell imaging showed a significant increase in abnormal divisions of confined cells across three different cell lines (HeLa, A375, and A549). Immunofluoresecence stains revealed a significant increase in cell diameter and chromosome area of confined cells, but no significant increase in centrosome-centromere distance upon division when compared to unconfined cells. The developed system could open up studies more broadly on confinement effects on mitotic processes, and increase the throughput of such studies.

2.1 Introduction

Chromosomal instability (CIN), characterized by rapid variations in chromosome number, is largely the result of chromosomal missegregation during mitosis. Inevitably, this

leads to aneuploidy, a significant hallmark of cancer[1]. This phenomenon has been induced experimentally and studied extensively through numerous avenues, including centrosome amplification[2–5], radiation[6], and DNA hypomethylation[7–9]. Yet, despite such studies, the mechanisms leading to the development of CIN *in vivo* have not been fully identified.

Recently, the influence of force balance on the proper segregation of chromosomes has been a subject of study. Under normal conditions, as cells enter M phase, the nuclear envelope and interphase microtubules (MT) disintegrate. Kinetochore microtubules (k-MT) extend from the centrosomes via various Ran GTPase-activated MT-associated proteins (MAPs)[10] and attach to the chromosome kinetochores through precise control of Aurora-B-kinase-dependent phosphorylation of Hec1[11]▪ , and regulation of small Rho GTPases such as Cdc42[12]. This is coupled with increased hydrostatic pressure[13] to drive cell rounding, as well as cortical cues, including force[14], that regulate local astral MT stability[15] which assist in positioning the centrosomes at opposite poles. The establishment of this bipolar spindle is followed by an alignment of the chromosomes at the spindle midzone, forming a metaphase plate[16]. The spindle assembly checkpoint (SAC), a complex, highly sensitive ensemble of proteins ensures that all of these steps have occurred properly before allowing progression into anaphase, where the spindle fibers draw the sister chromatids to opposite poles.

▪ Yet, external forces that can originate from the tumor microenvironment can disrupt these intricate mitotic processes. Previous studies have shown that cells that are uniaxially confined with stiff (~1 MPa) substrates display startlingly high frequencies of delayed mitosis, cell death, asymmetric division, cell fusion, and multi-polar cytokinesis[17], as illustrated in Fig. 1.

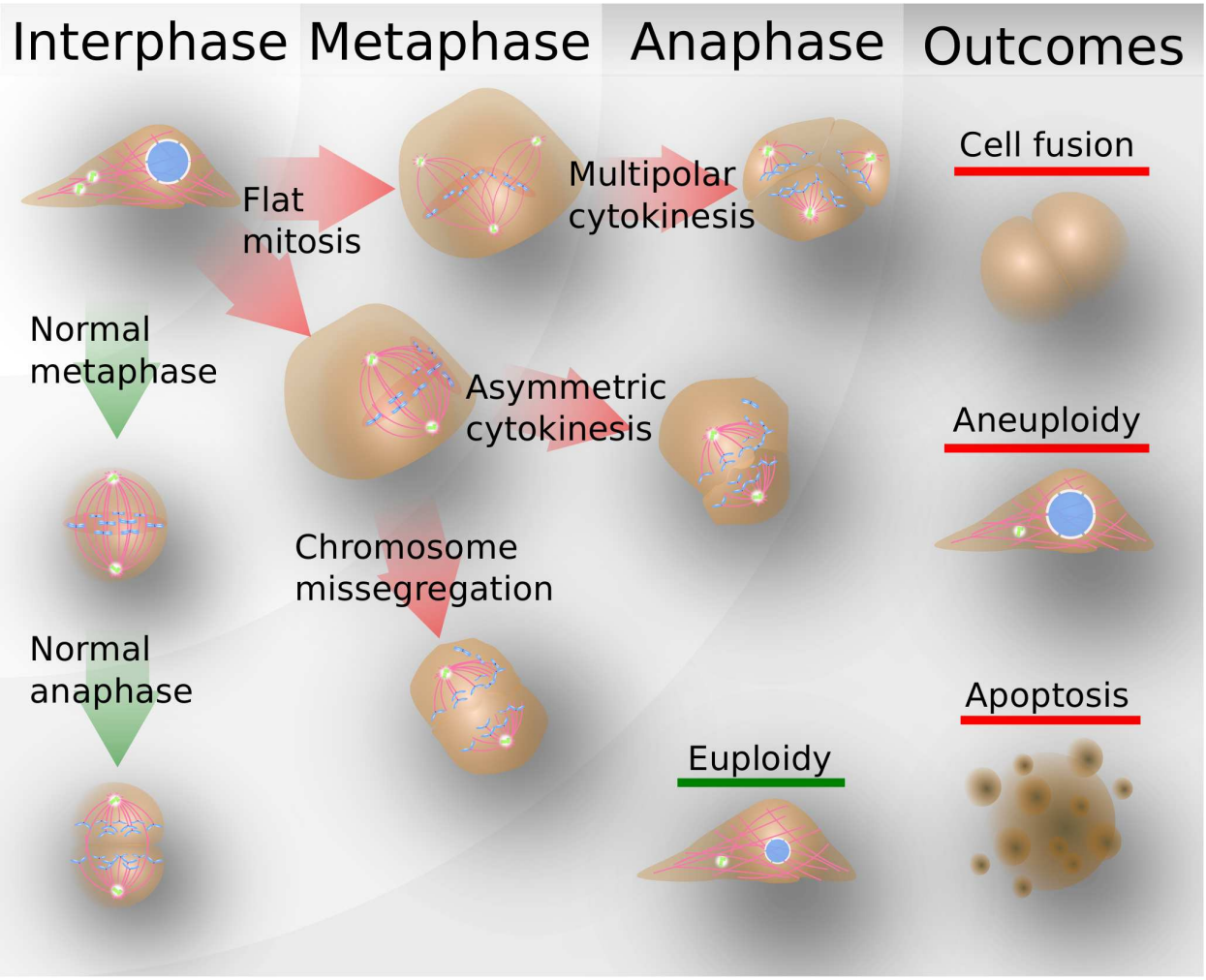

Figure 1: Mitotic progression of mechanically stressed cells. Flat divisions increase the frequency of chromosome missegregation, which can lead to asymmetric daughters and more than two daughter cells. If the cell remains viable, it is likely to be aneuploid, but in some cases daughters may fuse with each other or with neighboring cells.

The absence of sufficient space to establish proper cell rounding results in mitotic delays[17]; displacement of the chromosomes from proper metaphase alignment activates spindle assembly checkpoint proteins Bub1 and Mad1 to impede mitotic progression until alignment is signaled to be sufficient[18,19]. Prolonged exposure to such conditions appears to result in a decision at the cellular level down one of two routes: the cell may initiate apoptosis, or it may proceed through the checkpoint and attempt cytokinesis. The latter may occur, despite failure of

the k-MTs to gather all of the chromosomes to the metaphase plate, resulting in chromosome mis-segregation[19].

Depending on the location of formation of the spindle apparatus, the cell may initiate an uneven separation of its cytosol, producing daughters of significantly different sizes. In cells that contain additional centrosomes, which also establish poles by extending k-MTs to segregate chromosomes, more than two progeny can result – a process which is reduced in normal divisions where centrosomes can cluster at two poles symmetrically around a well-defined plane[2,3,20]. From any of these aberrations, the daughters are highly likely to carry aneuploid karyotypes. Yet another pathway exists, in which several or all of the daughter cells re-fuse, which may also produce aneuploid cells[21]. Severe aneuploidy may trigger apoptosis, but should the cells remain viable, they will carry their abnormal genetic material to the next cell cycle, which could lead to CIN and accelerate tumorigenesis.

The intracellular mechanisms of confined HeLa cells have been studied extensively by Lancaster et al[19]. Yet, many questions remain concerning mitotic processes during confinement, particularly the genes and protein localization that influence decisions such as: How is the metaphase plate assembled in such conditions? What influences the decision to proceed with an abnormal cytokinesis? What molecular or physical cues are at the top of the hierarchy of the assembly of the mitotic spindle apparatus? Additionally, confinement studies may shed more light into the fate of supernumerary centrosomes and the mechanisms behind formation of cleavage furrows in cells of flattened geometries. Finally, a solid connection to *in vivo* occurrences of confined cells of various tissue origins has yet to be established. Insights in how mitotic processes function in these perturbed conditions also enables a better understanding of

the machinery of normal mitotic processes and the strategies the cell uses to ensure the robustness of this process.

To better understand the fundamental intracellular mechanisms behind the impact of physical constraint on cell growth and division, we have developed an inexpensive and easy-to-use tool for confining a massive array of cells to pre-determined heights. It offers a unique advantage over other designs[17,22] in its simplicity and its ability to permit solution exchange. We describe methods of implementing this device for long-term live video capture, as well as for fluorescence staining and high resolution confocal imaging. As proof-of-concept, we applied the technology to perform confined culture of three cancer cell lines – HeLa, A549, and A375 – which are of varying origin, morphology, and genotype, and therefore display unique responses to confinement. HeLa cells are described as hypertriploid ($3N^{+}$), with 22-25 abnormal chromosomes out of a total of 76-80 chromosomes[23]. On the other hand, A375 and A549 cells are hypotriploid (3N), each with 60-63 chromosomes[24]. Furthermore, each of these cell lines is characterized by a unique set of losses and gains in chromosomes and chromosome regions.

2.2 Device Properties

We have developed a versatile system that enables reversible confinement of cells in a standard 12-well plate. Micropatterned devices were designed to establish a consistent cell confinement height in a vast array, segmented by feed channels for more uniform distribution of fresh nutrients to the culture. After experiments, the system can be disassembled, and the cells can be fixed, stained, and mounted to glass slides for long-term storage. This enables visualization and image analysis of large populations of dividing cells through confocal imaging, which shows the geometry and distribution of intracellular components during confinement.

2.2.1 PDMS Micropattern

The PDMS substrate for compressing cells was fabricated using standard soft lithography. The master mold was created using KMPR 1000 series [Microchem] negative photoresist. KMPR 1005 was spun at 2000 rpm for the first layer, corresponding to the for μm post confinement height. The subsequent 50 μm bypass channel layer was spun using KMPR 1050 at 2500 rpm.

2.2.2 Microfluidic insert

The full structure for a single well-plate insert consists of two poly-dimethylsiloxane (PDMS) components, and is illustrated in Fig. 2a. The bottom piece contains the micropattern, and was cured at a base:crosslinker ratio of 10:1 (~1 MPa) with a height of 1.5 mm and an inlet for media flow of 0.35 mm in diameter. The softer top component was cured at a 40:1 ratio to a height of 3 mm, with an 8 mm inlet. This soft piece serves as a gasket between the micropattern piece and the top compression plate. Both of these pieces were punched using a 17 mm core borer, and were permanently bonded together with air plasma [Harrick] in a configuration that left the micropattern on the external face to compress cells.

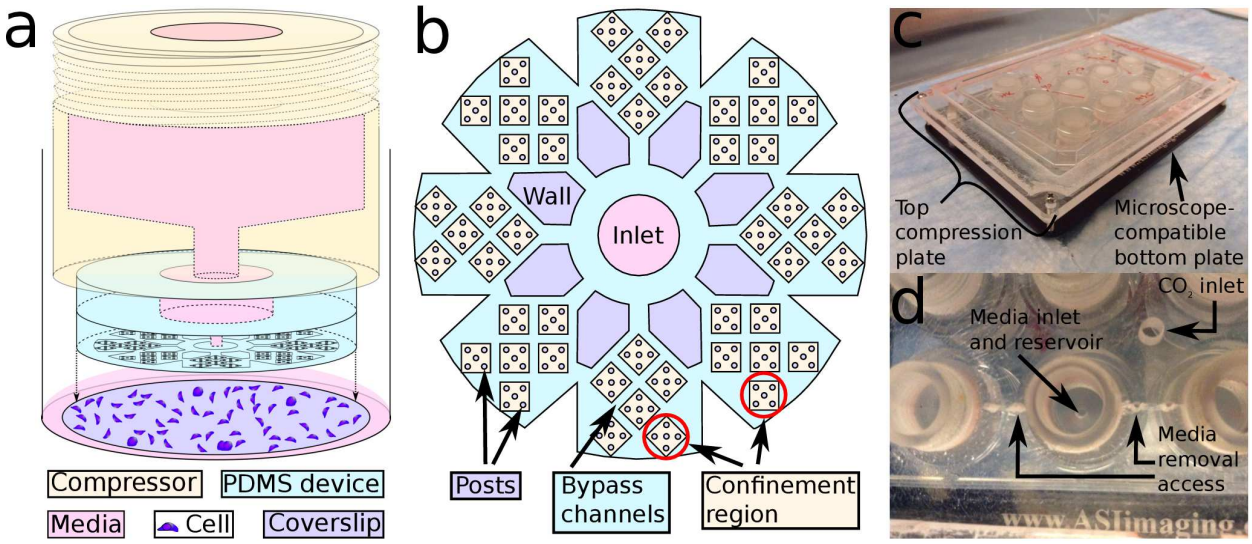

Figure 2: Schematic of the confinement insert. (A) The PDMS insert is adhered to the bottom of the screw-in well via the soft gasket layer, and is pressed evenly onto coverslips with a confluent cell culture. (B) Bottom-up view displays a micropattern that is placed on top of the cell culture. Solution flows from the central inlet via the bypass channels to evenly distribute into the array of confinement squares. (C) Full view and (D) zoomed-in view provide images of the compression plate and its features for maintaining optimum CO_2 and fresh media.

When the micropattern (Fig. 2b) is securely placed over the cells, media is flown through a single inlet in the center, which distributes fresh media to each confinement region via the bypass channels, and prevents drying. Posts are positioned within the confinement regions to prevent channel collapse. The array of confinement regions are designed to maximize the number of confined cells, while enabling the presence of the bypass channels of significantly larger height (50 µm) which also house the control group of unconfined cells. The 50 µm height of the bypass channels results in significantly lower fluidic resistance compared to the 7 µm height of the confinement region, thereby facilitating sufficient solution exchange throughout the device.

2.2.3 Confinement system

For a 12-well plate, we machined a confinement lid by inserting 12 screw-in polycarbonate reservoirs into a flat poly-methyl methacrylate (PMMA) piece. These reservoirs can each hold a maximum of 1.5 mL of media to gradually transfer to the confined cells. The

outer threading of the reservoir pieces allow adjustment of their heights in relation to the bottom of the well, if necessary. Twelve PDMS devices were autoclaved, and subsequently UV sterilized along with a vacuum chamber and the confinement plate. Each device was placed on the bottom of these reservoirs, taking advantage of the high adhesive strength of the gasket pieces. All parts of the system were placed in a sterile vacuum chamber to maintain sterility before confinement. Additionally, keeping the PDMS devices under vacuum minimized bubbles during confinement, and allowed better adhesion of the devices with the cover glasses at the bottom of the wells.

2.2.4 Cell culture

Prior to seeding, all coverslips were acid-cleaned, UV sterilized, plasma cleaned, and coated with 10 μg/mL of human plasma fibronectin. Three cell types from ATCC, HeLa cervical cancer, A375 melanoma, and A549 lung cancer were used in these studies. Upon reaching confluency, cells were passaged using conventional techniques and were reconstituted in the same volume of media. Roughly 5% of these cells were seeded onto the coverslips, which were placed in a 12-well plate for at least 2 hours to ensure uniform and confluent cell seeding. The cells were then subject to a double-thymidine block[25] to synchronize the cells at the interface of G1 and S phase, thereby facilitating the observation of mitotic cells. We observed significantly higher rates of cell death and asymmetric divisions, along with a significant reduction in multipolar divisions in HeLa cells that were untreated (Fig. 3). This suggests that delays in S phase resulted in supernumerary centrosomes, which increased the likelihood of more than 2 progeny. For consistency and as a proof-of-concept of the technology, we applied the double-thymidine block for all experiments.

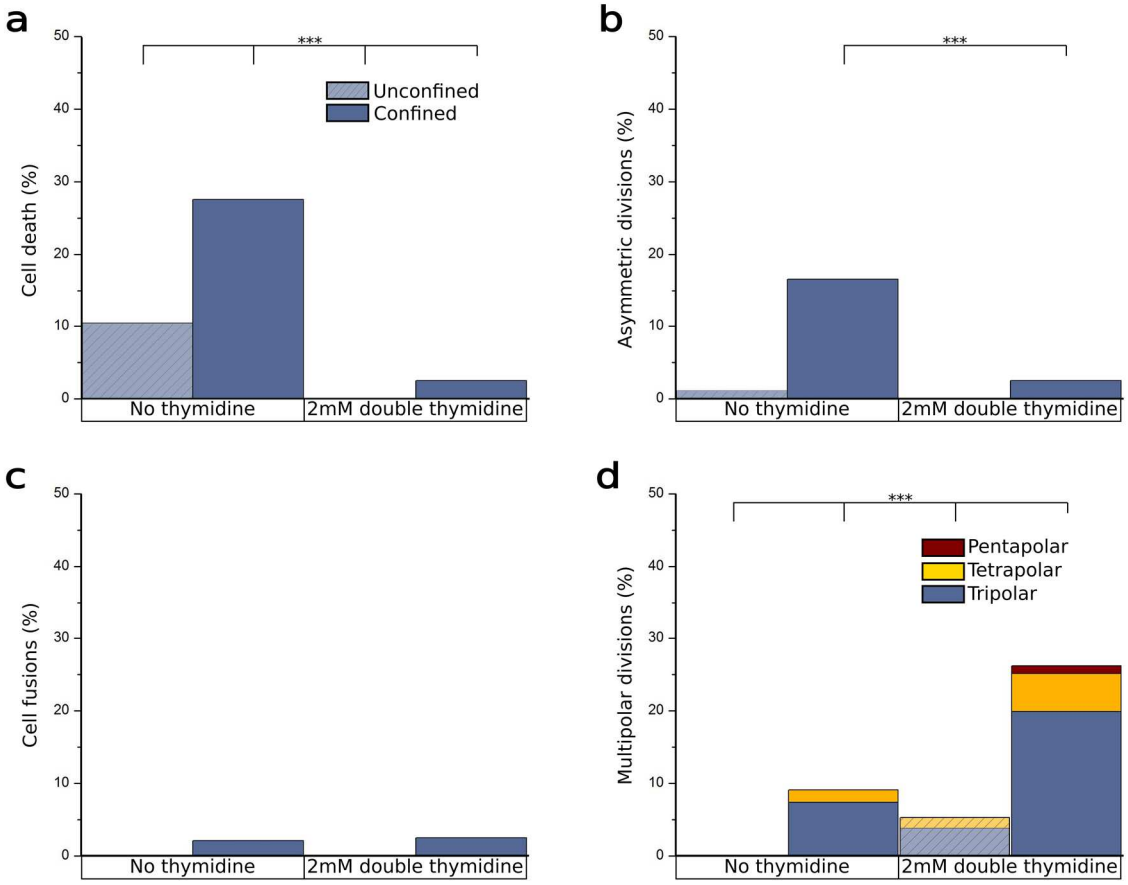

Figure 3: Comparison of anomalies for HeLa cells treated with a double thymidine block as opposed to cells with no treatment. Populations of confined HeLa cells were compared to unconfined cells for incidence of (a) cell death, (b) asymmetric divisions, (c) cell fusions, and (d) multipolar divisions (*** = $p<0.01$).

Upon release of this block, cells were confined. Cell density was quantified by the average cell matter coverage of the available confinement area. In A375 cells, we found that cell density >50% prevented cell flattening, and density <10% resulted in >90% cell death (data not shown), so for long-term confinement studies the cell densities for all lines were kept between 20-50%.

2.2.5 Confinement protocol

The 12-well plate containing the cell culture was secured into the microscope-compatible well-plate holder, as the compression plate was removed from desiccation. After ensuring that the inserts were securely fastened to the compression plate, the plate was lowered gently into the well plate as one piece, and the corners were screwed into the well-plate holder to maintain consistent compression over the course of the live-cell imaging experiments. The full protocol is detailed in Fig. 4.

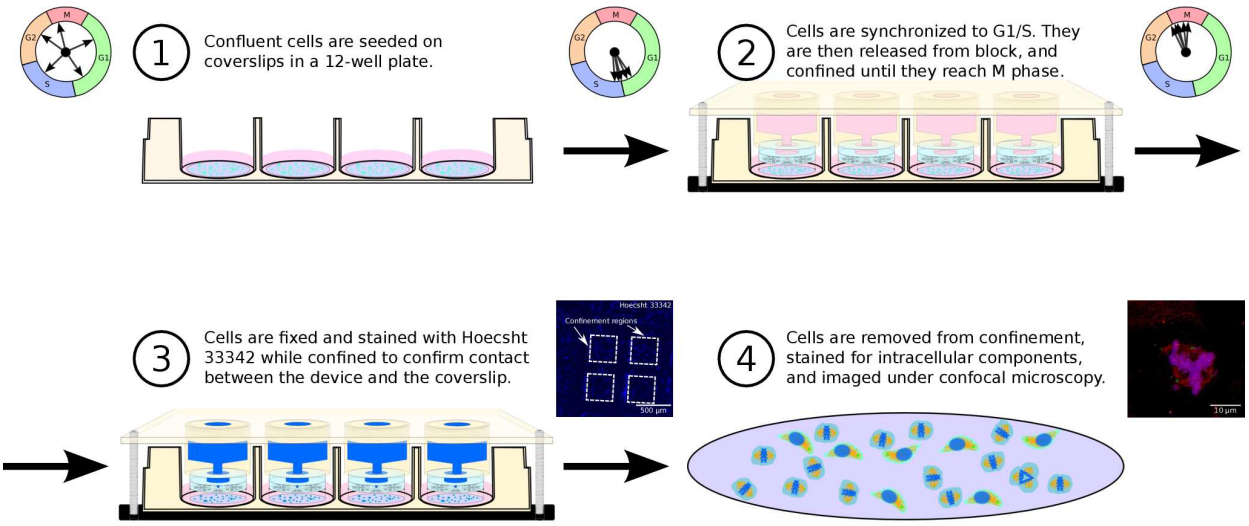

Figure 4: Experimental protocol for confining cells, and staining to maximize the visualization of mitotic events due to confinement.

2.2.6 Live imaging

To observe aberrant divisions occurring under confinement, the confinement platform was transferred to a fluorescence microscope [Nikon] with an incubated chamber set to 37°C and 5% CO_2. Multiple confinement regions were imaged every 10 minutes for 1-2 days, which was sufficient for obtaining a significant sample size of dividing cells. After the allotted time, 200 µL of 2 µM calcein AM and 4 µM ethidium homodimer was flowed through each inlet to ensure sufficient viability and as quality control to ensure that correct confinement was achieved. A

lack of uniform confinement could be confirmed by dye staining outside of the confined or bypass channel.

2.2.7 Data analysis

A sample of ≥140 cells were categorized for both the confined and unconfined cases. For each cell type, an approximate peak for cell divisions was determined within the duration of live imaging (data not shown), and was used as the optimum time for cell fixation and staining.

2.2.8 Immunocytochemistry

Cells were incubated under confinement at 37ºC and 5% CO_2. To increase the sample size of dividing cells to be visualized, the peaks times of cell division, determined from live imaging, were used as the duration of confinement in these experiments. At these peak times, 200 µL of fixation solution (4% formaldehyde, 1 µg/mL Hoechst,10 mM EDTA, 5 mM $MgCl_2$) was flowed through each inlet for 20 minutes to cross-link the cells and to simultaneously stain the nuclei. A nuclear stain (Hoechst 33342) was used to determine any leak into the walls of the channels, such that if the nuclei of cells did stain in the walls, then the inserts were deemed as improperly confined, and were excluded from further staining and analysis.

Cells were permeablized with 0.2% Triton X-100 for 20 minutes. After three PBS washes, coverslips were transferred to a petri dish [150 mm x 15 mm] on top of a paraffin sheet on top of a moist paper towel. This was done to reduce the volume of reagents required to perform ICC, and to prevent drying. Coverslips were treated with blocking solution (5% goat serum, 1% BSA, and 0.1% v/v Tween 20), followed by primary antibody incubation (blocking solution with 1:500 rabbit antipericentrin (Abcam, ab84542, lot GR30515), 1:250 chicken anti-alpha-tubulin (Abcam, ab89984, lot GR82981), 1:100 human anti-CREST (Antibodies Inc. 15-

234-0001, lot 1CK32)) and secondary antibody incubation (blocking solution with 1:500 goat anti-rabbit, 1:250 goat anti-chicken, and 1:100 goat anti-human). Each incubation was done for 1 hour at room temperature, with 3 blocking solution washes in between.

2.3. Results

2.3.1 Increased mitotic aberrations with confinement are cell line-dependent

Frequency and type of confinement-induced mitotic aberrations were cell line-dependent. Live cell brightfield time-lapse images enabled label-free quantification of aberrant divisions under confinement, as detailed in Fig. 5. At the normal end of the spectrum, A375 melanoma cells displayed the lowest frequency of aberrations, including multipolar divisions, asymmetric divisions, and fusions, though confined cells did have a significantly higher rate of such aberrations than unconfined cells. Yet, >45% of cells underwent cell death in both the confined and unconfined case (Fig. 5a). This may be because extreme delays in mitosis and improper chromosome segregation under confinement triggered intact mitotic checkpoints to initiate cell destruction, which may signal unconfined cells as well. In order of significantly increasing abnormalities, 9.8%, 14.2%, and 32.5% of confined A375, A549, and HeLa cells, respectively, produced asymmetric daughters (Fig. 5b, defined as divisions with >30% difference in size between any two daughters). Furthermore, while 5.7% of A375 cells produced three daughters, A549 and HeLa cells had an incidence of multi-polar divisions of 15.0% and 24.6%, respectively (Fig. 5d). A549 cells produced as many as four progeny, while HeLas produced as many as five. Correspondingly, HeLa cells had the lowest rate of cell death upon confinement, suggesting that these cells maintained the highest stability under these conditions. Interestingly, a statistically significant proportion of A549 cells fused upon division compared to the other lines (Fig. 5c), though for all cells this occurrence was rare (<11%).

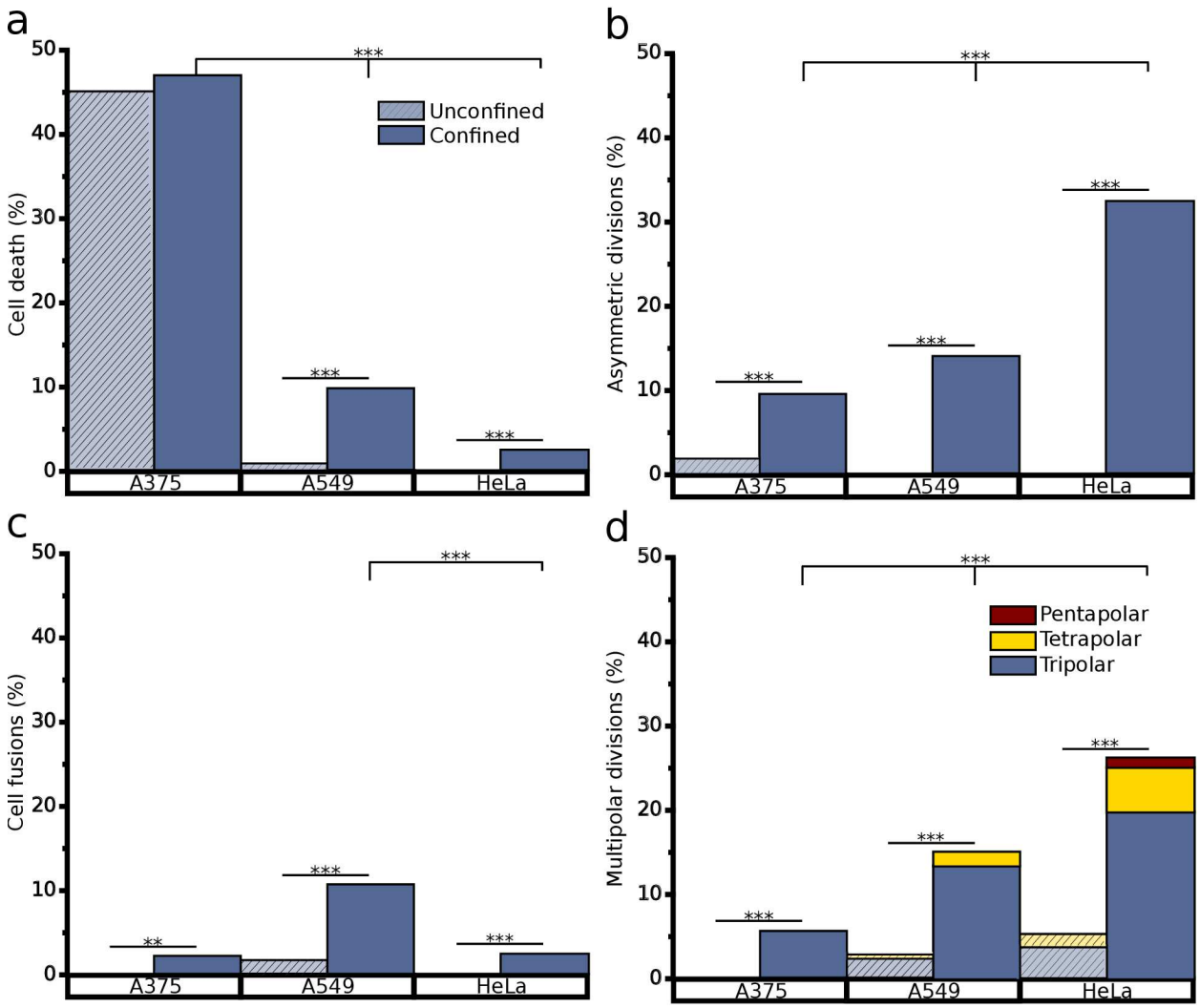

Figure 5: Occurrence of anomalies under confinement. Populations of confined A375, A549, and HeLa cells were compared to unconfined cells for incidence of (A) cell death, (B) asymmetric divisions, (C) cell fusions, and (D) multipolar divisions (** = $p < 0.05$ and *** = $p < 0.01$).

2.3.2 Confinement leads to splayed metaphase plates and chromosome mis-segregation

Confocal imaging of chromosomes, MTs, centrosomes, and centromeres revealed significant chromosomal spreading with conserved patterns defined by centrosome positioning and MT length (Fig. 6). Confined A375 cells in general possessed the least aberrant phenotypes as observed by immunofluorescence, matching the results from live cell imaging (Fig. 5). A375 cells form metaphase plates, but can fail to align some chromosomes, which were completely excluded from the spindle apparatus, but secured by polar astral MTs (Fig. 6a). In more common

cases, the chromosomes are within the reach of the dynamic MTs, but may align parallel to them (Fig. 6b). We identified more pronounced segregation anomalies in A549 cells, where many confined cells showed a large splaying of DNA such that the metaphase plate formed in the plane of confinement. Fig. 6c contains many cells in late anaphase or telophase, where the chromosomes have segregated, but this may suggest a positioning of the centrosomes to ideal locations. This is further evidenced by Fig. 6d, which shows a high magnification asymmetric tri-daughter A549 division. Higher order multipolar cytokinesis events were commonly observed in confined HeLa cells, including tetradaughter divisions (Fig.6e) and rare pentadaughter divisions (Fig. 6f). In both cases, we see radially symmetric MT extensions with relatively uniform lengths emerging from the centrosomes. Chromosome locations appear to correspond with the limits of radial extension of MTs and display similar symmetry. The centrosomes in these multi-daughter divisions appear less punctate (Fig. 6e, f), which may be due to clustering of several centrosomes. In the case of the penta-daughter division (Fig. 6f) centrosomes occupy five optimal positions that permit equidistant extension of MTs to the kinetochores. Cells with supernumerary centrosomes can assume a variety of configurations for spindle stabilization (Fig. 6g, h). For example, in Fig. 6h the pentapolar spindle consists of a central cluster of centrosomes that complements four other equidistant pole. HeLa cells are not limited to pentapolar spindles; we do report the observation of a higher-order configuration, but at that stage, it becomes difficult to accurately visualize the exact number of poles.

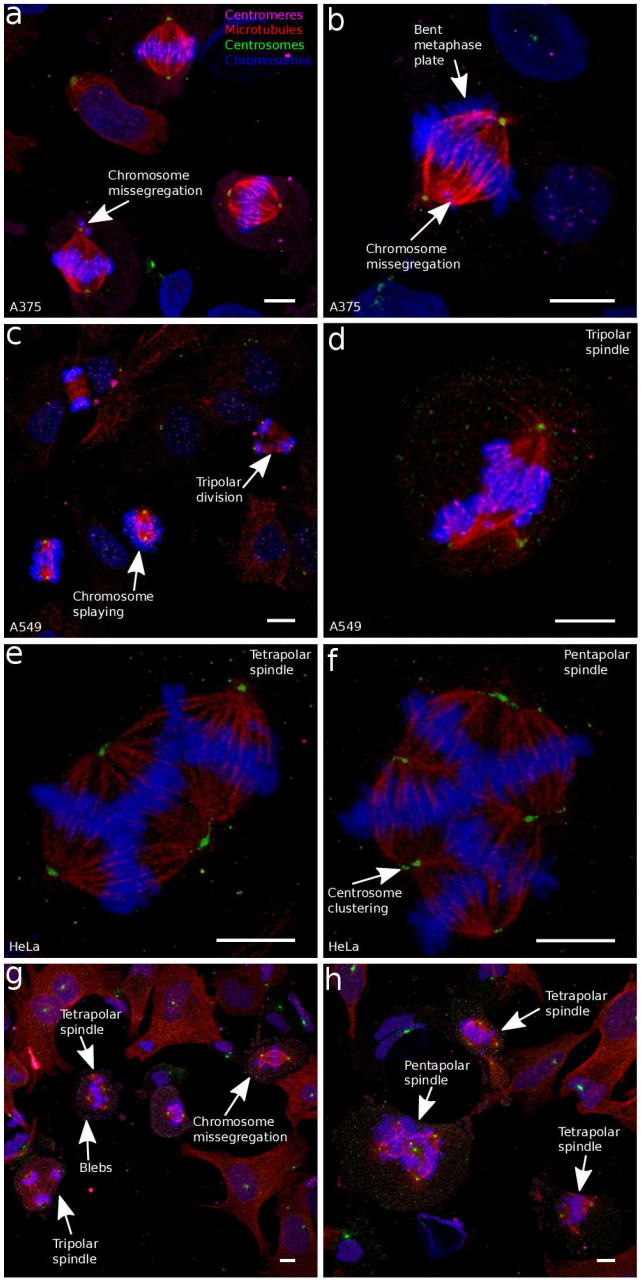

Figure 6: Immunofluorescence stains of confined cells reveal a variety of mitotic aberrations. (A-B) show A375 cells that form metaphase plates, but failed to align all chromosomes. (B) shows a more pronounced form where much of the DNA has oriented abnormally in a plane that is co-planar with the MTs. (C-D) shows A549 cells undergoing chromosomal splaying and tridaughter divisions. (C) identifies a cell that is attempting to segregate chromosomes that are closer to its astral microtubules. The other cells appear to be in late anaphase or telophase, where the DNA is beginning to reach the centrosomes. (D) reveals a tridaughter division where the attachment of the microtubules to the kinetochores implies asymmetric arrangement of the chromosomes. (E-F) are singular images of the most extreme cases of flat mitosis in HeLa cells, where cells are undergoing (E) tetrapolar and (F) pentapolar divisions. (G-H) show the full range of aberrant multi-daughter asymmetric divisions, chromosome missegregation, and plasma membrane blebbing in HeLa cells.

We next evaluated whether confined cells extended microtubules over longer distances to compensate for their elongated shapes during mitosis. To do this, we characterized the degree of flattening of confined and unconfined HeLa cells (Fig. 7a), as well as the maximal distance between centrosomes and centromeres (Fig. 7b). Confined cells show an 87.4% increase in cell area, and a 13.3% increase in centrosome-centromere distance, confirming that the cells are being significantly flattened although modification of position of the centrosomes is minor. Though not statistically significant ($p < 0.1$), the additional distance that the MT must extend in confined cells may be enough to account for the chromosome missegregation that we observe. Average chromosome area in the XY plane increased by 38.5%, while average circularity decreased by 37.3% in confined cells. These results were also only significant at $p < 0.1$ level, which was expected as chromosome density still remains constant and z-height reduction is assumed to be uniform.

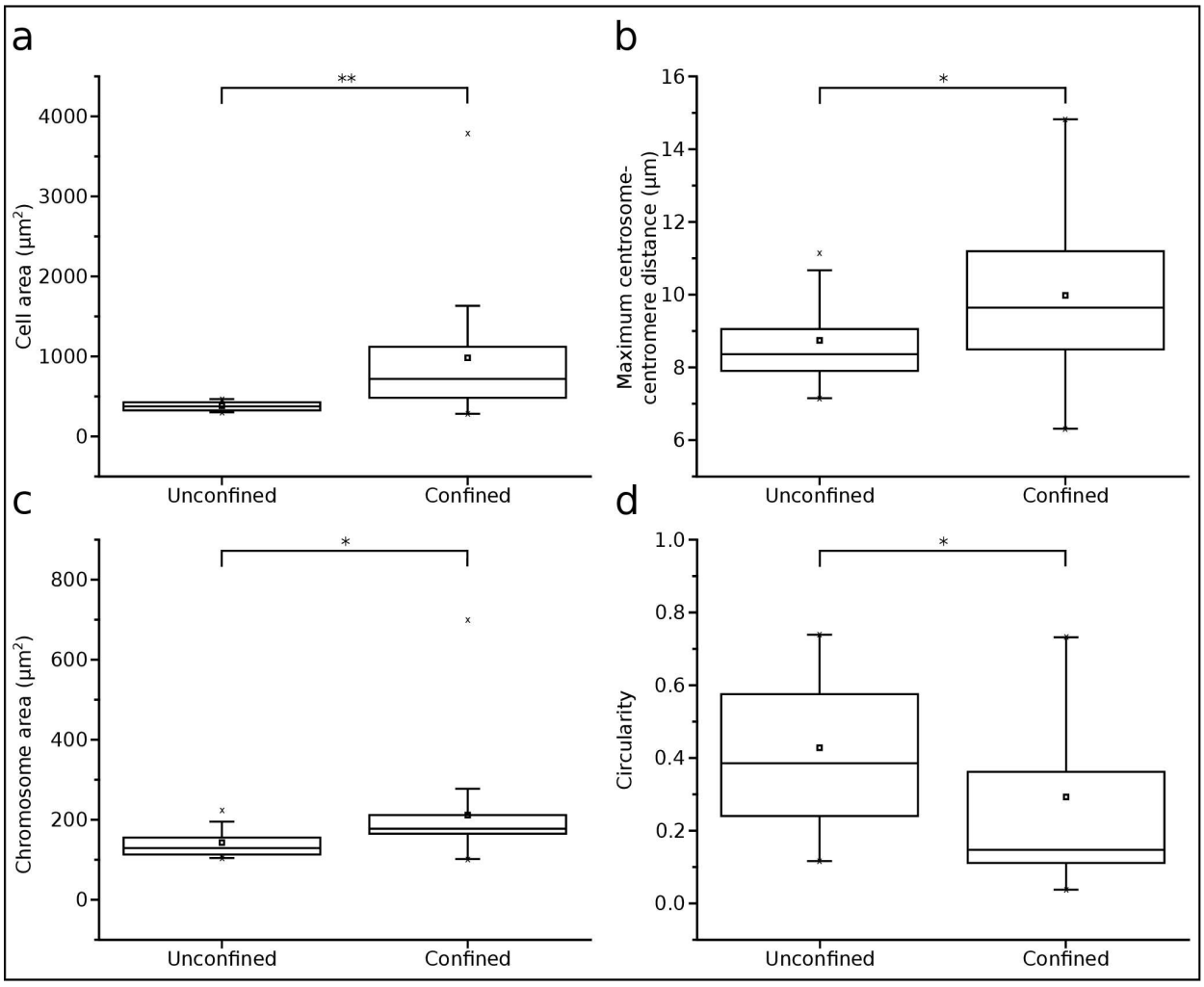

Figure 7: Confined and unconfined HeLa cells are compared in the XY plane in terms of (A) cytosolic area, (B) circularity, (C) maximum centrosome-centromere distance, and (D) chromosome area. Confined cells display significant increases in cytosolic area, and slight increases in DNA area and centrosome-centromere distance, as well as a slight decrease in circularity.(* = $p < 0.10$ and ** = $p < 0.05$).

$$C = \frac{4\pi A}{p^2} \quad (1)$$

where C is circularity,

A is area, and

p is perimeter.

Because the increased hydrostatic pressure of mitotic cells is insufficient to displace the stiff substrate, the acto-myosin cortex is forced to take on an irregular configuration. As shown in Fig. 7d, there was no significant increase in maximum centrosome-centromere distance. From this, we can infer that the maximum distance of required microtubule extension is conserved and largely independent of the overall cell shape, a similar result to what has been described in recent literature[19,26–28].

2.4 Discussion

The variation of aberration frequency across cell lines may result from a vast number of genomic differences among them. Spectral karyotyping of HeLa and A549 reveal drastic differences in individual chromosome number and translocations[23,24]. Pre-existing mutations in the SAC will facilitate the initiation of anaphase despite chaotic conditions. Average centrosome number of the population will influence the rate of onset of multipolar configurations. A549 cells have been documented as having multiple centrosomes in 46% of its population[29]. Furthermore, for multipolar divisions, copy number for each chromosome will influence the viability of daughter cells. For example, while HeLa is considered to be a hypertriploid line (3n+), A549 and A375 are hypotriploid (3n-) [ATCC], which may partially explain why HeLa cells were more likely to generate viable multidaughter progeny. Although the HeLa cell line has been sequenced, A549 has not, and further detailed genomic sequencing data would be required to elucidate molecular mechanisms responsible for the different behaviors between cell lines under confinement.

Another key result is the fairly consistent length of microtubules, independent of cell diameter during division. The conserved microtubule lengths, even for higher order multipolar divisions, appears to be enabled by coordinated positioning of the centrosomes. Previous works

seem to agree that in the presence of supernumerary centrosomes, the dividing cell spends a majority of mitosis in a stable multipolar configuration[3,20], most likely due to the establishment of sufficient tension of the kinetochore-attached MTs, which widens the spatial separation of aurora B kinase from its kinetochore substrates[30]. This causes a reduction in phosphorylation of kinetochore substrates, and fulfills the SAC checkpoint of stabilized microtubule-kinetochore attachment[30]. As part of this stabilization, non-kinetochore microtubules (those that extend to the midzone without binding to kinetochores) then contribute polar ejection forces[31,32] to chromosome arms, which orient the chromosomes at the metaphase plate. However, in response to multipolar configurations, it is clear that unusual metaphase plates are produced (Fig. 6e-f).

To produce viable progeny, these multipolar configurations and unusual metaphase plates must then form abnormal cleavage furrows[33] during subsequent cytokinesis. Though cleavage onset is beyond the scope of this study, we report unusual observations for daughter cell separation under confinement. As opposed to the normally circular, symmetric divisions, confined cell daughters tend to separate abruptly, sometimes ejecting bleb-like structures. Even in confined cells that underwent bipolar symmetric divisions, cleavage was misshapen. Several models of cleavage furrow placement have been proposed, yet there is currently no prevalent theory on the exact underlying mechanisms[34]). Though our findings do not directly support any model over another, our confinement system may be used as a rapid method for inducing unusual cleavage furrows. Induction of offset metaphase plates (as seen in bipolar asymmetric divisions) or unusual metaphase plate geometries (as seen in multipolar divisions) in high throughput may assist in developing a better understanding of the level of contribution of different types of MTs to cleavage formation[34,35].

Though multi-polar mitotic events were rare in A375 cells, we were surprised to find that the frequency was greatly increased with a reduction in confinement height. Cells that remained viable after being subjected to near-zero height were significantly more likely to undergo higher order multidaughter divisions (Fig. 8). The presence of multiple centrosomes in such levels of confinement were absent from confinement at 7 μm, which may suggest that centrosome amplification is a cellular response to limited space and subsequent splaying of chromosomes. Borel, et al. give evidence to support the idea that supernumerary centrosomes arise from an override of the tetraploidy checkpoint and failure to arrest in G1[2], which may potentially be induced by abnormal spindle formation from increasing levels of confinement, followed by progression into the next cell cycle. Interestingly, Hut, et al. report that when DNA is improperly replicated or is damaged, there is an increased likelihood of centrosome splitting into multiple structures that contain single centrioles[36]. The level of confinement in these A375 cells is sufficient to induce lamina rupture[22], which may trigger centrosome splitting and multipolar cytokinesis. However, a true understanding of the mechanisms behind this phenomenon will require further studies of these cells under several well-controlled heights. Though our previous confinement approach explored the impact of lower confinement heights on HeLa cells[17], our current device can ensure a more uniform height with higher N that can be compatible with long-term fluorescent live-cell imaging to facilitate tracking of centrosome duplication or splitting.

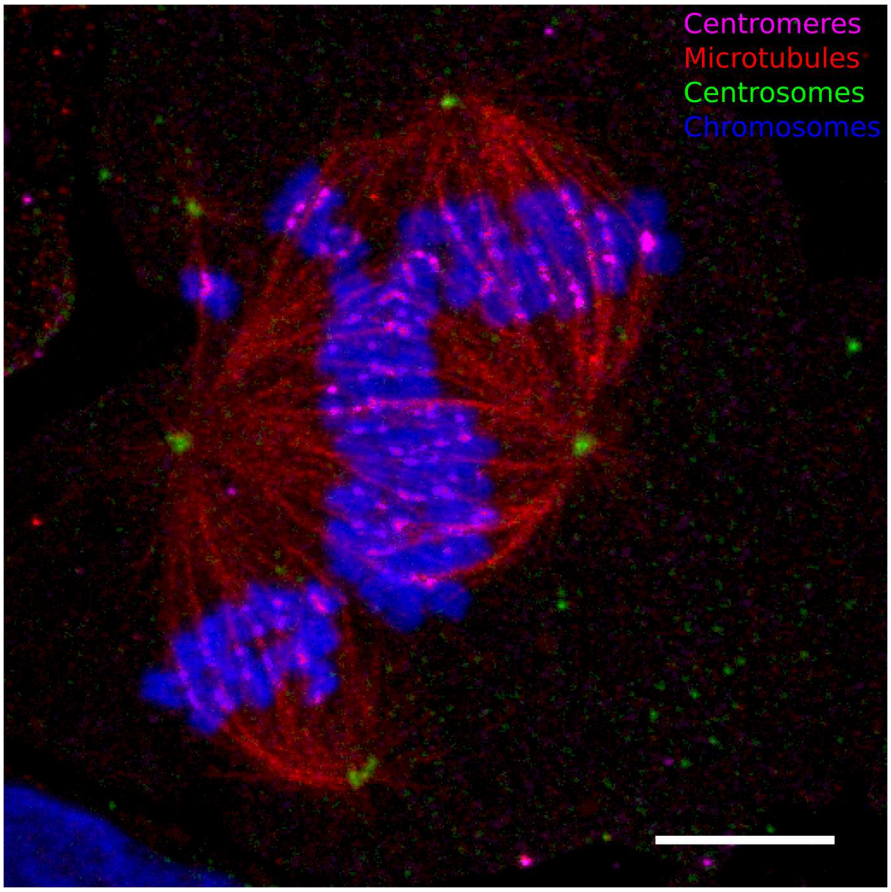

Figure 8: Rare pentapolar configuration for an A375 cell that was maximally confined. This cell was surrounded by several other higher-order multipolar configurations, whereas fixed cells that had been subjected to 7 μm confinement revealed no multipolar cells. Scalebar = 10 μm.

2.5 Conclusion

We have developed a platform that permits long-term studies of physical disruption of spindle assembly and chromosome segregation on a large number of cells in parallel. It offers the unique advantages of simplicity of use with standard cell culture and well-plate formats, as well as uniform distribution of any media or solution to be used in tandem with confinement experiments. We have shown that cells of varying genetic makeup, origin, and morphology differ in response to confined conditions. This technology may serve as a reliable method for cell biologists to study more specific genetic pathways involved in mitosis and response to confinement.

2.6 Acknowledgements

The authors would like to thank Yeganeh Amini, Coleman Murray, and Nikhil Kalluri for their assistance in this work. Confocal laser scanning microscopy was performed at the CNSI Advanced Light Microscopy/Spectroscopy Shared Resource Facility at UCLA, supported with funding from NIH-NCRR shared resources grant (CJX1-443835-WS-29646) and NSF Major Research Instrumentation grant (CHE-0722519).

2.7 References

1. Gordon, D. J., Resio, B. & Pellman, D. Causes and consequences of aneuploidy in cancer. *Nat. Rev. Genet.* **13,** 189–203 (2012).
2. Borel, F., Lohez, O. D., Lacroix, F. B. & Margolis, R. L. Multiple centrosomes arise from tetraploidy checkpoint failure and mitotic centrosome clusters in p53 and RB pocket protein-compromised cells. *Proc. Natl. Acad. Sci.* **99,** 9819–9824 (2002).
3. Ganem, N. J., Godinho, S. A. & Pellman, D. A mechanism linking extra centrosomes to chromosomal instability. *Nature* **460,** 278–282 (2009).
4. Lingle, W. L. *et al.* Centrosome amplification drives chromosomal instability in breast tumor development. *Proc. Natl. Acad. Sci.* **99,** 1978–1983 (2002).
5. Pihan, G. A., Wallace, J., Zhou, Y. & Doxsey, S. J. Centrosome abnormalities and chromosome instability occur together in pre-invasive carcinomas. *Cancer Res.* **63,** 1398–1404 (2003).
6. Limoli, C. L., Kaplan, M. I., Giedzinski, E. & Morgan, W. F. Attenuation of radiation-induced genomic instability by free radical scavengers and cellular proliferation. *Free Radic. Biol. Med.* **31,** 10–19 (2001).
7. Menendez, L., Benigno, B. B. & McDonald, J. F. L1 and HERV-W retrotransposons are hypomethylated in human ovarian carcinomas. *Mol. Cancer* **3,** 12 (2004).
8. Nishigaki, M. *et al.* Discovery of aberrant expression of R-RAS by cancer-linked DNA hypomethylation in gastric cancer using microarrays. *Cancer Res.* **65,** 2115–2124 (2005).

9. Wilson, A. S., Power, B. E. & Molloy, P. L. DNA hypomethylation and human diseases. *Biochim. Biophys. Acta BBA-Rev. Cancer* **1775,** 138–162 (2007).
10. Hetzer, M., Gruss, O. J. & Mattaj, I. W. The Ran GTPase as a marker of chromosome position in spindle formation and nuclear envelope assembly. *Nat. Cell Biol.* **4,** E177–E184 (2002).
11. DeLuca, K. F., Lens, S. M. & DeLuca, J. G. Temporal changes in Hec1 phosphorylation control kinetochore–microtubule attachment stability during mitosis. *J Cell Sci* **124,** 622–634 (2011).
12. Yasuda, S. *et al.* Cdc42 and mDia3 regulate microtubule attachment to kinetochores. *Nature* **428,** 767–771 (2004).
13. Stewart, M. P. *et al.* Hydrostatic pressure and the actomyosin cortex drive mitotic cell rounding. *Nature* **469,** 226–230 (2011).
14. Tseng, P., Judy, J. W. & Di Carlo, D. Magnetic nanoparticle–mediated massively parallel mechanical modulation of single-cell behavior. *Nat. Methods* **9,** 1113–1119 (2012).
15. Théry, M. *et al.* The extracellular matrix guides the orientation of the cell division axis. *Nat. Cell Biol.* **7,** 947–953 (2005).
16. Ditchfield, C. *et al.* Aurora B couples chromosome alignment with anaphase by targeting BubR1, Mad2, and Cenp-E to kinetochores. *J Cell Biol* **161,** 267–280 (2003).
17. Tse, H. T. K., Weaver, W. M. & Di Carlo, D. Increased Asymmetric and Multi-Daughter Cell Division in Mechanically Confined Microenvironments. *PLoS ONE* **7,** e38986 (2012).
18. Itabashi, T. *et al.* Mechanical impulses can control metaphase progression in a mammalian cell. *Proc. Natl. Acad. Sci.* **109,** 7320–7325 (2012).
19. Lancaster, O. M. *et al.* Mitotic Rounding Alters Cell Geometry to Ensure Efficient Bipolar Spindle Formation. *Dev. Cell* **25,** 270–283 (2013).
20. Krämer, A., Maier, B. & Bartek, J. Centrosome clustering and chromosomal (in) stability: a matter of life and death. *Mol. Oncol.* **5,** 324–335 (2011).
21. Lu, X. & Kang, Y. Cell fusion as a hidden force in tumor progression. *Cancer Res.* **69,** 8536–8539 (2009).

22. Le Berre, M., Aubertin, J. & Piel, M. Fine control of nuclear confinement identifies a threshold deformation leading to lamina rupture and induction of specific genes. *Integr. Biol.* **4,** 1406 (2012).
23. Macville, M. *et al.* Comprehensive and definitive molecular cytogenetic characterization of HeLa cells by spectral karyotyping. *Cancer Res.* **59,** 141–150 (1999).
24. Luk, C., Tsao, M. S., Bayani, J., Shepherd, F. & Squire, J. A. Molecular cytogenetic analysis of non-small cell lung carcinoma by spectral karyotyping and comparative genomic hybridization. *Cancer Genet. Cytogenet.* **125,** 87–99 (2001).
25. Sanchez, I., Goya, L., Vallerga, A. K. & Firestone, G. L. Glucocorticoids Reversibly Arrest Rat Hepatoma Cell Growth by Inducing an Early G 1 Block in Cell Cycle Progression. *Cell Growth Differ.* **4,** 215–215 (1993).
26. Good, M. C., Vahey, M. D., Skandarajah, A., Fletcher, D. A. & Heald, R. Cytoplasmic volume modulates spindle size during embryogenesis. *Science* **342,** 856–860 (2013).
27. Hazel, J. *et al.* Changes in cytoplasmic volume are sufficient to drive spindle scaling. *Science* **342,** 853–856 (2013).
28. Wühr, M. *et al.* Evidence for an upper limit to mitotic spindle length. *Curr. Biol.* **18,** 1256–1261 (2008).
29. Jiang, F., Caraway, N. P., Li, R. & Katz, R. L. RNA silencing of S-phase kinase-interacting protein 2 inhibits proliferation and centrosome amplification in lung cancer cells. *Oncogene* **24,** 3409–3418 (2005).
30. Liu, D., Vader, G., Vromans, M. J., Lampson, M. A. & Lens, S. M. Sensing chromosome bi-orientation by spatial separation of aurora B kinase from kinetochore substrates. *Science* **323,** 1350–1353 (2009).
31. Antonio, C. *et al.* Xkid, a chromokinesin required for chromosome alignment on the metaphase plate. *Cell* **102,** 425–435 (2000).
32. Rieder, C. L. & Salmon, E. D. Motile kinetochores and polar ejection forces dictate chromosome position on the vertebrate mitotic spindle. *J. Cell Biol.* **124,** 223–233 (1994).

33. Wheatley, S. P. & Wang, Y. I. Midzone microtubule bundles are continuously required for cytokinesis in cultured epithelial cells. *J. Cell Biol.* **135,** 981–990 (1996).
34. Burgess, D. R. & Chang, F. Site selection for the cleavage furrow at cytokinesis. *Trends Cell Biol.* **15,** 156–162 (2005).
35. Alsop, G. B. & Zhang, D. Microtubules are the only structural constituent of the spindle apparatus required for induction of cell cleavage. *J Cell Biol* **162,** 383–390 (2003).
36. Hut, H. M. *et al.* Centrosomes split in the presence of impaired DNA integrity during mitosis. *Mol. Biol. Cell* **14,** 1993–2004 (2003).

Chapter 3: Probing cell adhesion profiles with a microscale adhesive choice assay

The last chapter investigated the aberrant phenotypes that develop in mechanically deformed aneuploid cells. In this chapter, we move from biological discovery and into the use of phenotypic phenomena as a means of characterizing cells by type. Mammalian cell adhesion to the extracellular matrix influences numerous physiological processes. Current *in vitro* methods to probe adhesion focus on adhesive force to a single surface, which can investigate only a sub-component of the adhesive, motility, and polarization cues responsible for adhesion in the three-dimensional tissue environment. Here, we demonstrate a method to quantify the adhesive properties of cells that relies on the microscale juxtaposition of two ECM-coated surfaces. By multiplexing this approach, we investigate the unique adhesive profiles for breast cancer cells that are adapted to colonize different metastatic sites. We find that malignant breast cancer cells readily transfer to new collagen I surfaces, and away from basement membrane proteins. Integrins and actin polymerization largely regulate this transfer. This tool can be readily adopted in cell biology and cancer research to uncover novel drivers of adhesion (or de-adhesion) and sort cell populations based on complex phenotypes with physiological relevance.

3.1 Introduction

Physical interactions of mammalian cells with their microenvironment influences numerous key cellular functions such as motility, growth, survival, and differentiation. In cancer, invasion and metastasis are likely underpinned by abnormal adhesive programs, which allow cells to colonize and spread along new extracellular matrix (ECM) compositions that differ from the original tissue structure, following the seed-to-soil hypothesis. In this hypothesis, tumor cell

"seeds" settle in microenvironments with the most suitable "soil"[1–3] through favorable soluble and adhesive interactions.

In breast cancer patients, mortality is largely due to metastases from the primary tumor to secondary sites such as bone[5–7], lung[8], and brain[9,10] tissue, each with unique ECM[4]. However, current tumor cell analysis often fails to predict propensity for metastasis. For a localized tumor, current prognostic markers are insufficient to confidently assess metastatic risk in 70 % of all breast cancer patients[4]. Secondary site prediction markers are especially in demand, furthering the need for new quantitative and high-throughput techniques to analyze biopsied cells. Molecular analysis tools have shed some light on the expression level changes of adhesion proteins for site-specific metastatic cells. For example, cells that metastasize to bone tend to overexpress the osteopontin gene[11], while those that metastasize to lung have increased expression of tenascin C[12].

These promising gene-expression signatures for breast tumors may be complemented with novel phenotypic biomarkers for a wide range of physical properties associated with metastasis such as deformability[13,14], size[15], contractility[16], or adhesion[17]. Identifying cells that adhere to microenvironments with specific morphology, forces, ECM type, and ECM density may be particularly useful for determining likely metastatic destinations in breast cancer[17].

Previous technologies to characterize cell adhesion have led to quantitative measures of adhesion strength[18]. Many of these adhesion-based characterization tools rely on attaching cells to 2D surfaces which do not activate the dorsal ligands[19], and therefore do not represent the morphology and migration of cells *in vivo*[20] where cells receive chemical cues from all directions[21,22].

Here we present a multiplexed transhesion platform that sandwiches cells between different ECM protein-coated surfaces to determine a "relative adhesive signature". This format allows multi-directional exposure of cells to ECM, which, in comparison to 2D surfaces, can better model the 3D *in vivo* environment with ECM degradation activity, cell motility, and cell adhesion that is involved in metastatic spread. We determined that cells with mesenchymal phenotype can transfer away from an originally-seeded surface and adhere to a new surface, a process we term "transhesion". We find that transhesion is largely dictated through actin polymerization, integrin composition, and potentially ECM degradation. Using the same mechanisms, we demonstrate the ability to enrich cell subpopulations by their unique transhesive characteristics, which may enable subsequent physical or genetic characterization with increased signal-to-noise in the future[15,23].

3.2 Results

3.2.1 Transhesion concept and workflow

The fundamental idea is to expose a population of cells to two different surfaces, and then carefully separate those two surfaces and count where cells remain attached. As shown in Figure 1a, cells are seeded onto a surface coated in ECM protein 1, and are sandwiched in a standard 60 mm petri dish against a top surface coated in ECM protein 2. Each surface is composed of a glass backbone and a thin layer of PDMS micropatterned with large 5 micron deep trenches to safely house the cells under a consistent 10 micron compression height (Fig. 1b, Fig. 2a), such that cells can engage both surfaces in a uniform manner. Due to differences in a combination of factors which may include integrin densities, spread area, matrix metalloprotease (MMP) production, migration rate, or integrin binding strength, cells will have higher overall affinity to

one ECM-coated surface over another. Upon separation of the surfaces, the region is imaged and the percentages of cells that remained and transferred are quantified.

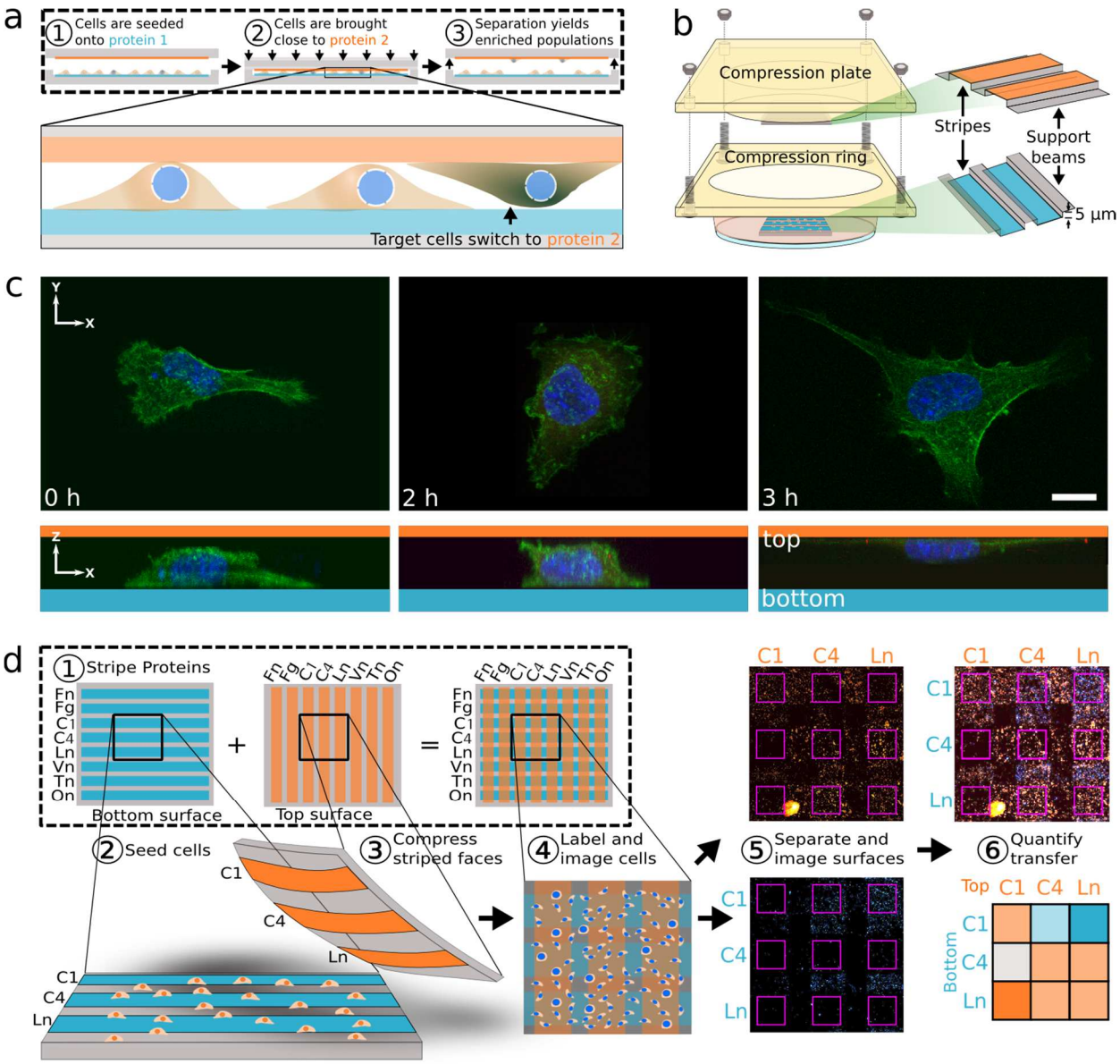

Figure 1: Mechanism of transhesion. (a) A cell population is seeded onto a surface coated in protein 1. After 2 hours, cells adhered to protein 1 are introduced to a new surface coated in protein 2. Cells are given 3 hours to adhere more strongly to one or the other of the two surfaces, after which the surfaces are separated. (b) The transhesion platform is constructed around a standard 60 mm diameter petri dish. A thin layer of cured 40:1 PDMS is placed on the inside of the petri dish and the inside of the compression plate. Each surface comprises a thin (40-60 µm) layer of patterned PDMS with a 5 µm trench height over a 1 mm thick glass backbone. Proteins are coated in the trenches, and the two surfaces are compressed such that trenches are orthogonally arranged. Support beams prevent collapse, maintaining an even 10 µm height over the 2 mm x 2 mm compression regions of interest. (c) Confocal images showing the top view and cross section as cells transhere from a bottom Ln coated surface to a top C1 coated surface over 3 hours. Nucleus (blue) is stained with Hoescht 33342 and actin cytoskeleton is labeled with phalloidin. (d) Proteins were striped in parallel lanes in the multiplexed format where eight orthogonally oriented stripes on the top and bottom produce 64 combinations of ECM pairs for testing. Cells were labeled with nuclear stain (Hoechst 33342) and live-dead stain, and surfaces were imaged during compression and after separation. Cells were enumerated on each separated surface to produce heat maps showing percentage of transfer to the top surface for each protein pair. Darker orange indicates proclivity to the top surface while darker blue indicates cell preference to adhere to the bottom surface.

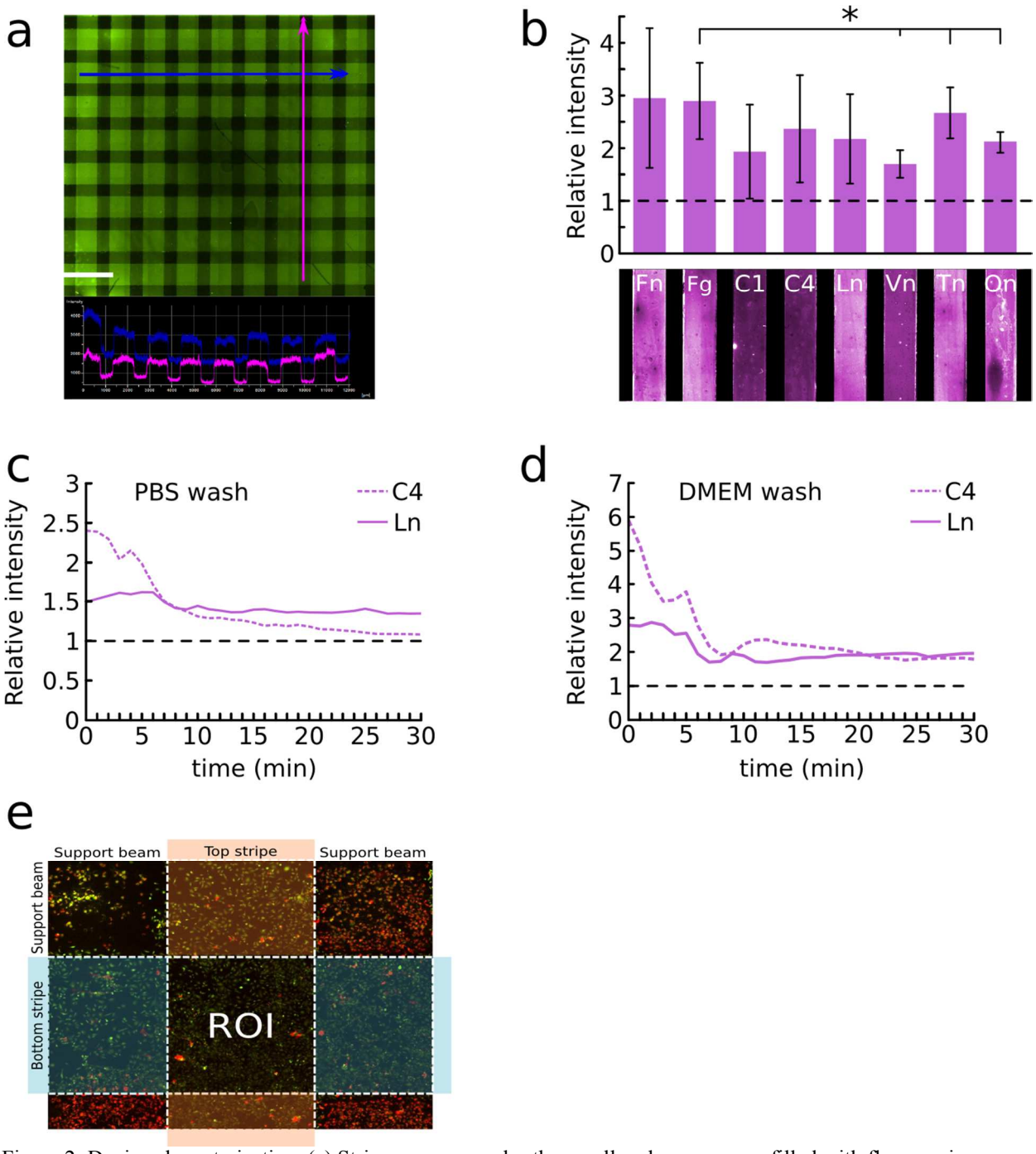

Figure 2: Device characterization. (a) Stripes compressed orthogonally where gaps are filled with fluorescein solution yielded an even intensity distribution indicating uniform compression. Scale bar is 5 mm. (b) After coating the substrate with APTES, eight fluorescently labeled ECM proteins are striped along channels at 100 µg/mL for 1 hour. All stripes were washed with 1xPBS prior to intensity measurements. Aside from vitronectin (Vn), ECM proteins displayed similar levels of fluorescence. *P<0.05. Degradation of C4 and Ln stripes over time is measured when the surface is washed with (c) PBS or (d) DMEM, which shows that intensities tend to stabilize at roughly 10 minutes for each wash. (e) Regions of interest are measured at the intersection of protein stripes. For convention, bottom stripes run horizontally while top stripes run vertically.

The assay is simply multiplexed using protein stripes orthogonally arranged between the bottom and top surfaces (Fig. 1d). Cells were subjected to combinatorial pairs of 8 different ECM proteins that were coated along the micro-trenches in parallel stripes (Methods). Intensity readouts of fluorophore-conjugated proteins coated on the treated surfaces confirm electrostatic adsorption of the proteins after washing (Fig. 2b). Regions of interest (ROIs) were identified by the intersections of these stripes (Fig. 2c), and upon surface separation, cells were enumerated in each ROI of the top and bottom surface. The resulting percent transfer to the top surface for each ROI was plotted as heatmaps, where orange indicates high transhesion, and blue indicates low transhesion (see Methods for more details).

Using the platform, we tested 5 different breast cell lines. The human mammary epithelial cells (hMEC) were used as a control for non-transformed breast cells. We also used the well-studied MDA-MB-231 line, and 3 tropic MDA-MB-231 lines – TGL/1833 (bone tropic), TGL/4175 (lung tropic), and TGL/Brm-2a (brain tropic) – as developed by Joan Massague's lab[5,8,10] and henceforth referred to as MDA-bone, MDA-lung, and MDA-brain, respectively. Figure 1c shows confocal cross-sections of MDA-lung cells that are fixed between a collagen I (C1)-coated top surface and an uncoated bottom surface at different durations to see the progression of transhesion. All sandwich experiments were performed for 3 hours. However, for cells compressed for durations other than 3 hours, we found fairly consistent percentages of transhesion, including short time periods like 30 minutes (Fig 3).

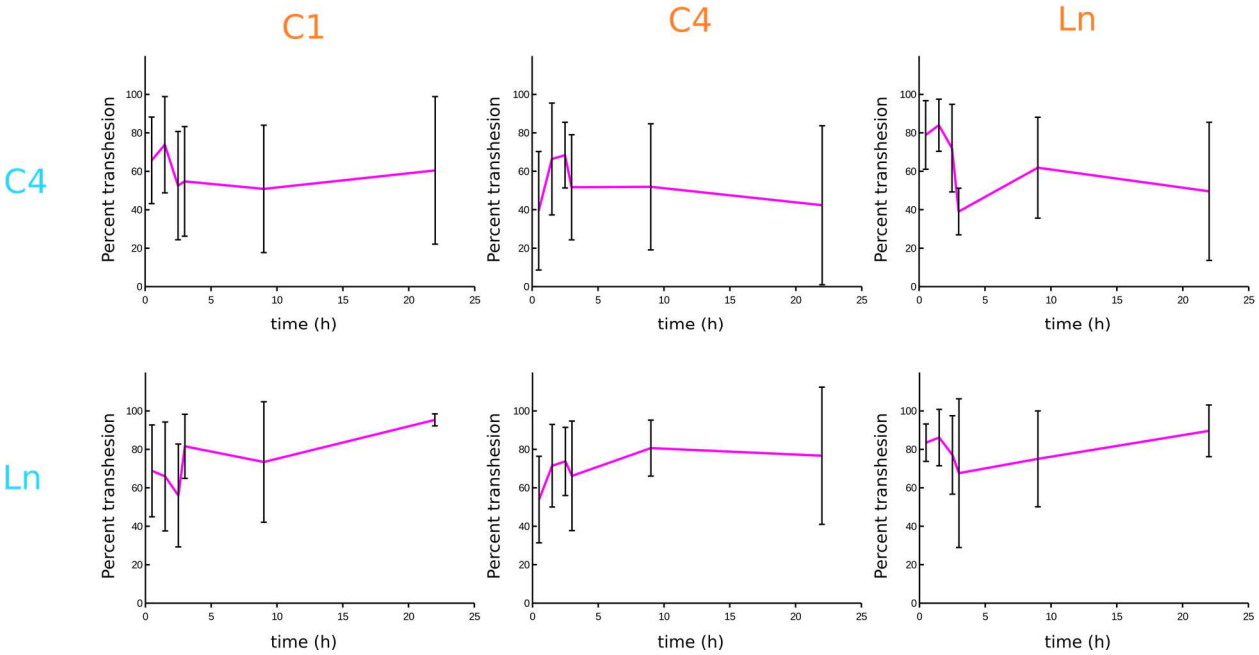

Figure 3: Cell transhesion for different confinement durations in six different protein pair combinations.

In a competition between the same ECM proteins, we find that MDA-lung cells display a consistent transfer rate to the top when observing cell numbers above 100 (Fig. 4a). Similarly, hMEC viability is stable beyond 100 cells per region of interest (Fig. 4b), so we performed all experiments with a minimum of 100 cells. Transhesion is dependent on protein concentration for some ECM proteins (Fig. 4c), but it appears to be uninfluenced by gravitational effects (Fig. 4d). However, for convention, cells are always seeded on the bottom surface and are given the opportunity to transfer to a new top surface.

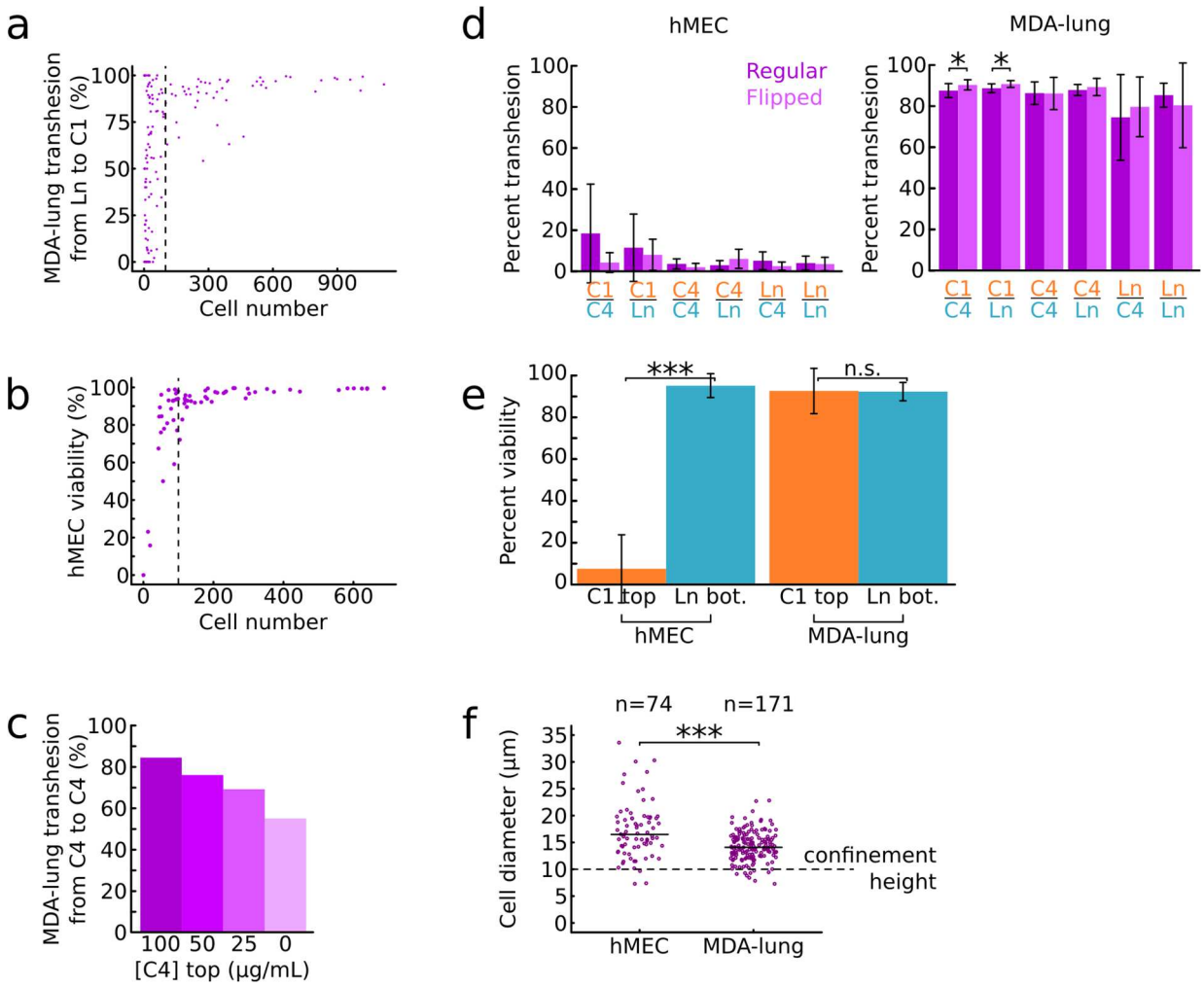

Figure 4: Cell behavior in the transhesion platform. (a) MDA-lung transhesion from Ln to C1 is plotted with respect to cell number. Below ~ 100 cells per experiment data remains noisy. (b) hMEC viability on the bottom surface is measured with respect to cell number in the condition of C1 (top) and Ln (bottom). (c) MDA-lung transhesion is measured from C4 at 100 µg/mL to C4 surfaces of varying concentrations. (d) Gravitational effects are measured for MDA-lung cell transhesion from Ln to C1 by having cells start on the top as opposed to the bottom surface. n=12. (e) Cell viability of hMEC and MDA-lung is measured for cells on top and bottom surfaces after transhesion from Ln to C1. (f) Cell diameter for hMEC and MDA-lung. Confinement height is 10 µm. *P<0.01, **P<0.005, and ***P<0.001.

3.2.2 Mesenchymal phenotypes may promote breast cell transhesion to introduced collagen I surfaces

Using the multiplexed mode, we profiled the 5 different breast cell lines (Fig. 5) to identify distinct behaviors among those cells. We first notice that collagen I (C1) had a strong tendency to attract all types of MDA-MB-231 cells to the top surface. However, hMECs do not transfer to the top surface regardless of the presented protein. Furthermore, viability of MDA-lung cells remaining on either surface after separation was above 90 %, but only viability of hMEC on their initial Ln coated surface was above 90 % (Supplementary Fig. 2e).

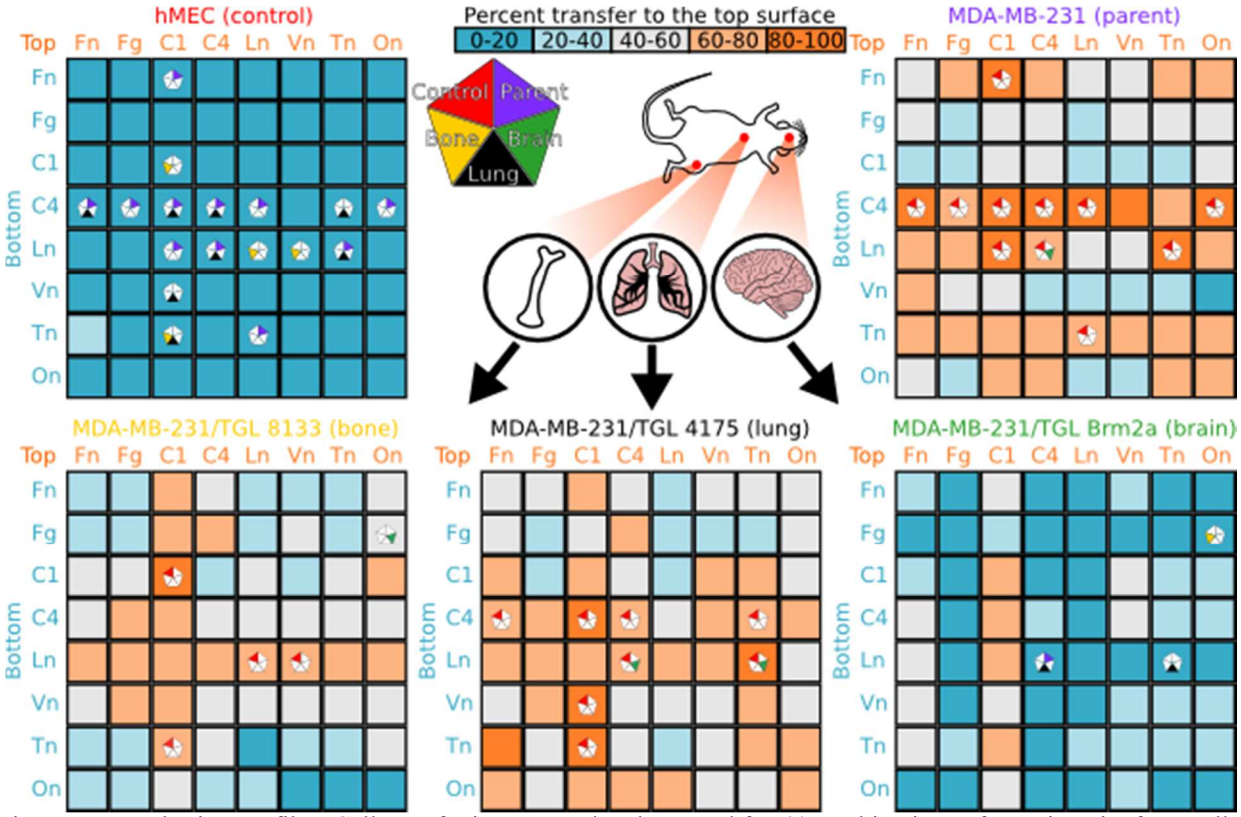

Figure 5: Transhesion profiles. Cell transfer is measured and mapped for 64 combinations of protein pairs for 5 cell lines: hMEC (control non-cancerous breast epithelial cells), MDA-MB-231 (parent malignant mesenchymal cells), and metastatic MDA cells that are characterized to have tropism to bone, lung, or brain. Darker orange squares indicate a larger percentage of transfer to the top while darker blue squares indicate smaller percentage of transfer to the top. For each protein pair and cell line with significant differences in transfer between cell lines, pentagons are shown, with colored wedges indicating P-values < 0.01. Two sample test of proportion with n >800 cells over 6 experiments.

To help explain these differences in transhesion, we first looked at the morphological features of hMEC and MDA-lung cells remaining on each surface after being subjected to 6 different combinations of protein pairs: C1vC4 (collagen IV), C1vLn, C4vC4, C4vLn, LnvC4, and LnvLn. A higher spread area and lower circularity usually corresponds to the formation of strong adhesions on a surface that allow for force generation, polarization, and spreading of the cell[24] on a 2D surface. The hMEC cells are larger than MDA-lung cells on average (Fig. 4f), and so their spread area tends to be slightly larger for most conditions (Fig. 6b). Additionally, hMEC typically have high circularity (Fig. 6c), which is slightly reduced when they spread on a top C1 surface. Conversely, MDA-lung cells form pseudopodia which increase their spread area (Fig. 6f) and have sharply lower circularity (Fig. 6g) after transhering to the top C1 surface.

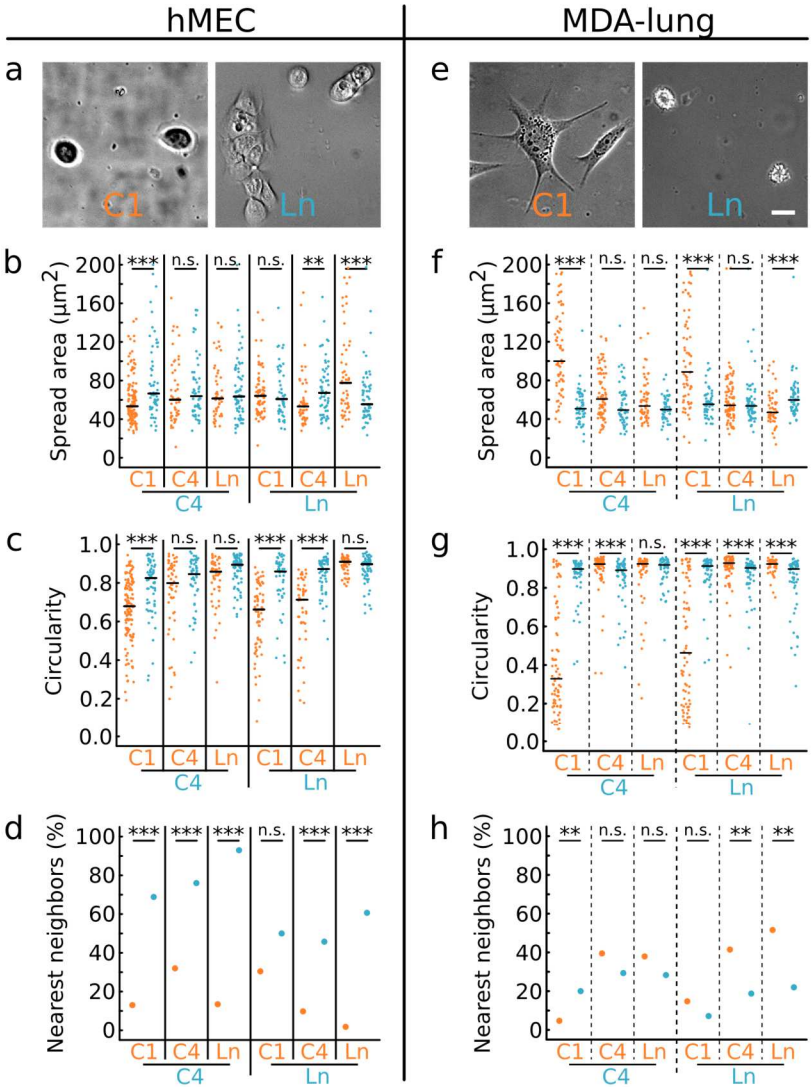

Figure 6: Cell morphology of epithelial hMEC and mesenchymal MDA-lung cells for six ECM pair conditions correlated with transhesion. (a, e) representative images of cells spread on a C1 coated top surface and a Ln coated bottom surface. Scale bar is 10 μm. Cell spread area (b, f) and circularity (c, g) measurements highlight MDA-lung cell commitment and polarization on top C1 surfaces in the platform. (d, h) hMEC remaining on the bottom surface tended to share edges with other cells, indicating stronger preference to form cell-cell adhesions on their initially seeded surface as opposed to transhering. n≥50 cells. *P<0.01, **P<0.005, and ***P<0.001.

For all conditions, hMEC remaining on the bottom surface were significantly more likely to share edges with adjacent cells (Fig. 6d), while MDA-lung cells spread out without significant cell-cell contact (Fig. 6h). Analysis of vimentin and E-cadherin expression, which are markers of mesenchymal and epithelial phenotypes, respectively, shows pronounced levels of vimentin in MDA-lung cells, and punctate staining of E-cadherin at the edges of hMECs, as expected (Fig. 7). Taken together, general proclivity to C1, combined with mesenchymal-like traits that reduce cell-cell contacts, may correlate with enhanced ability to transfer to C1.

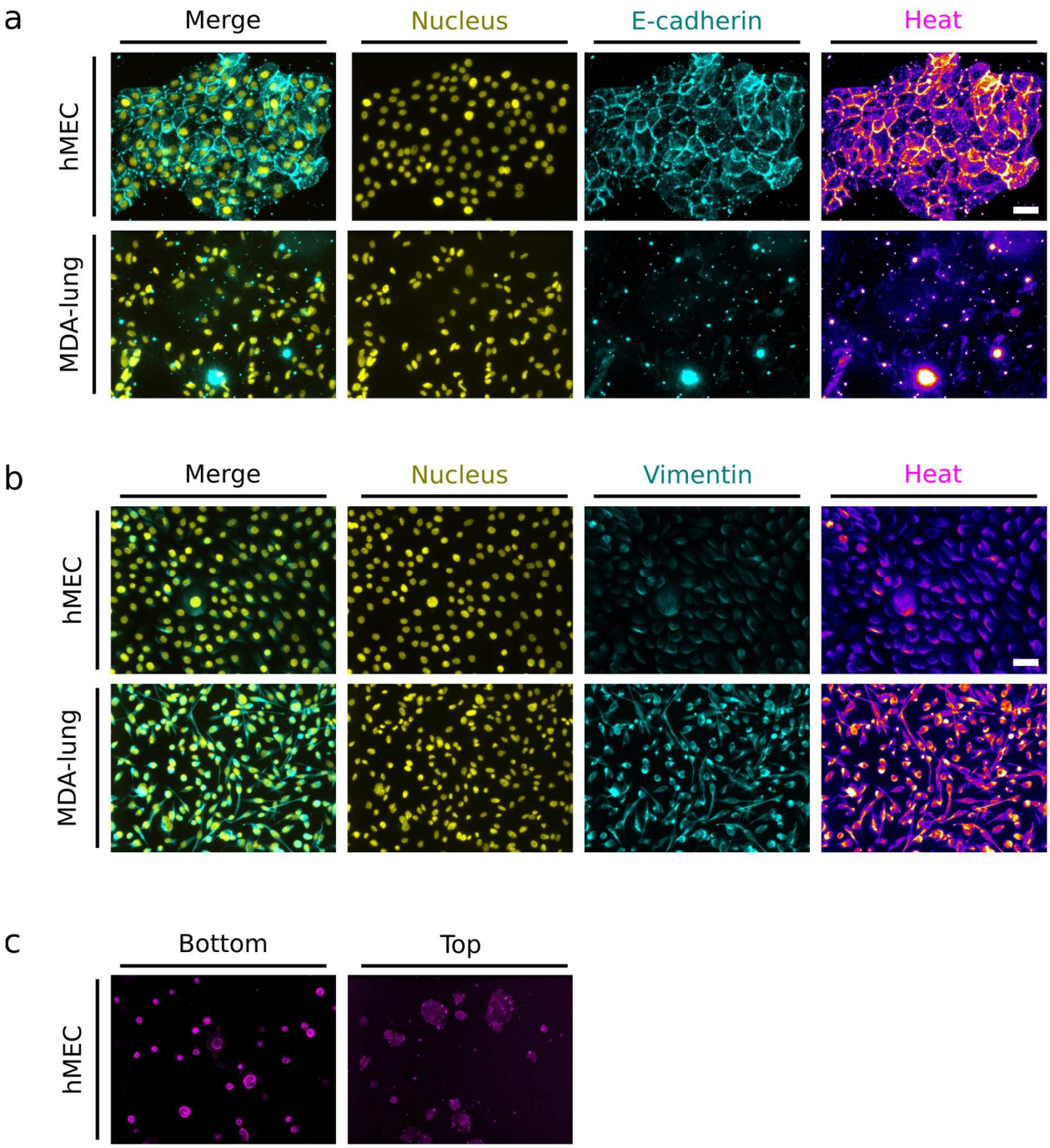

Figure 7: hMEC and MDA-lung cells are stained for (a) E-cadherin and (b) vimentin on a 2D surface. (c) E-cadherin staining of hMEC on a bottom Ln coated surface and a top C1 coated surface after transhesion show significant decrease in intensity at the periphery of cells that transhered to the top. Scale bar is 50 μm.

3.2.3 Cell transhesion may be largely dictated by integrin expression and actin assembly

To understand molecular mechanisms contributing to transhesion, we investigated the roles of several cellular components in mediating MDA-lung cell transhesion from one surface to another when subjected to the same 6 ECM protein pair conditions used in Figure 6. We first looked into integrins, which are heterodimeric transmembrane proteins that allow cells to interact with ECM directly. In our analysis of integrin binding, we investigated the ubiquitous β1 integrin subunit, as well as α6 and α2 due to their known interactions with laminin and collagens, respectively. Cells were seeded for the normal duration of 2 hours, and were then dosed with blocking antibodies to α2, α6, and β1 for 30 minutes. Antibodies to α2 and β1 knocked down transfer to the top surface (Fig. 8, Fig. 9) while populations treated with α6 antibodies retained the ability to transfer for all protein pairs.

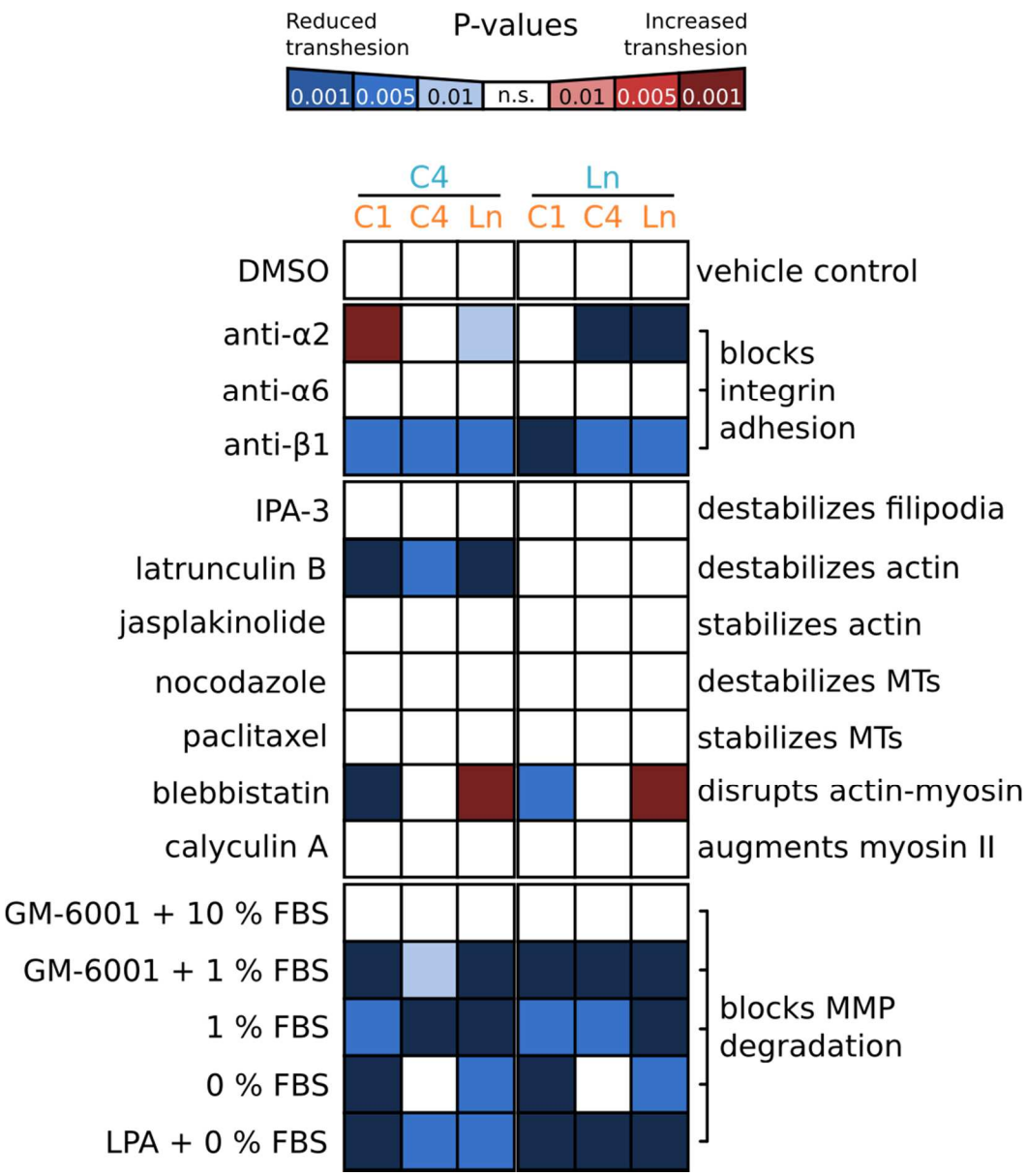

Figure 8: Mechanisms of transhesion for MDA-lung cells. Transhesion was observed for cells exposed to six ECM pair conditions and pharmacological and antibody-based inhibition of integrin, filopodia, actin, microtubule, myosin, or MMP function. Transhesion knockdown was observed for cells treated with α2 integrin, β1 integrin, latrunculin B, blebbistatin, and DMEM with reduced FBS. n >3 for all drug and antibody treatments, and n>125 for MDA-lung control experiments.

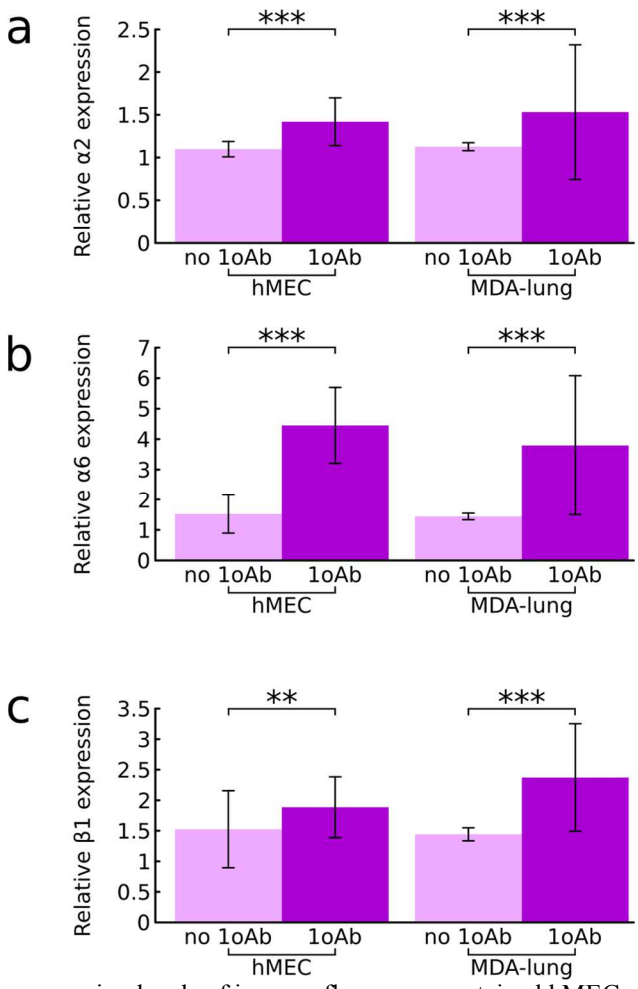

Figure 9: Relative integrin expression levels of immunofluorescence-stained hMECs and MDA-lung cells with antibodies against (a) α2, (b) α6, and (c) β1 integrins. n>45. **P<0.005 and ***P<0.001.

In addition to observing the effects of blocking several integrin components, we found that modulating several intracellular cytoskeletal proteins in MDA-lung cells affected transhesion for several competing ECM-coated surfaces (Fig. 8, Fig. 10). After MDA-lung cells were dosed with latrunculin B, an actin-destabilizing drug, cell transfer was dramatically reduced when cells started on a C4 surface. Interestingly, blebbistatin, which disrupts actin-myosin interactions, appeared to knockdown transfer to a C1 surface, but slightly increase transfer to a Ln surface. Other drugs we tested that modulate microtubule assembly and breakdown suggest that these processes do not play a dominant role in transhesion.

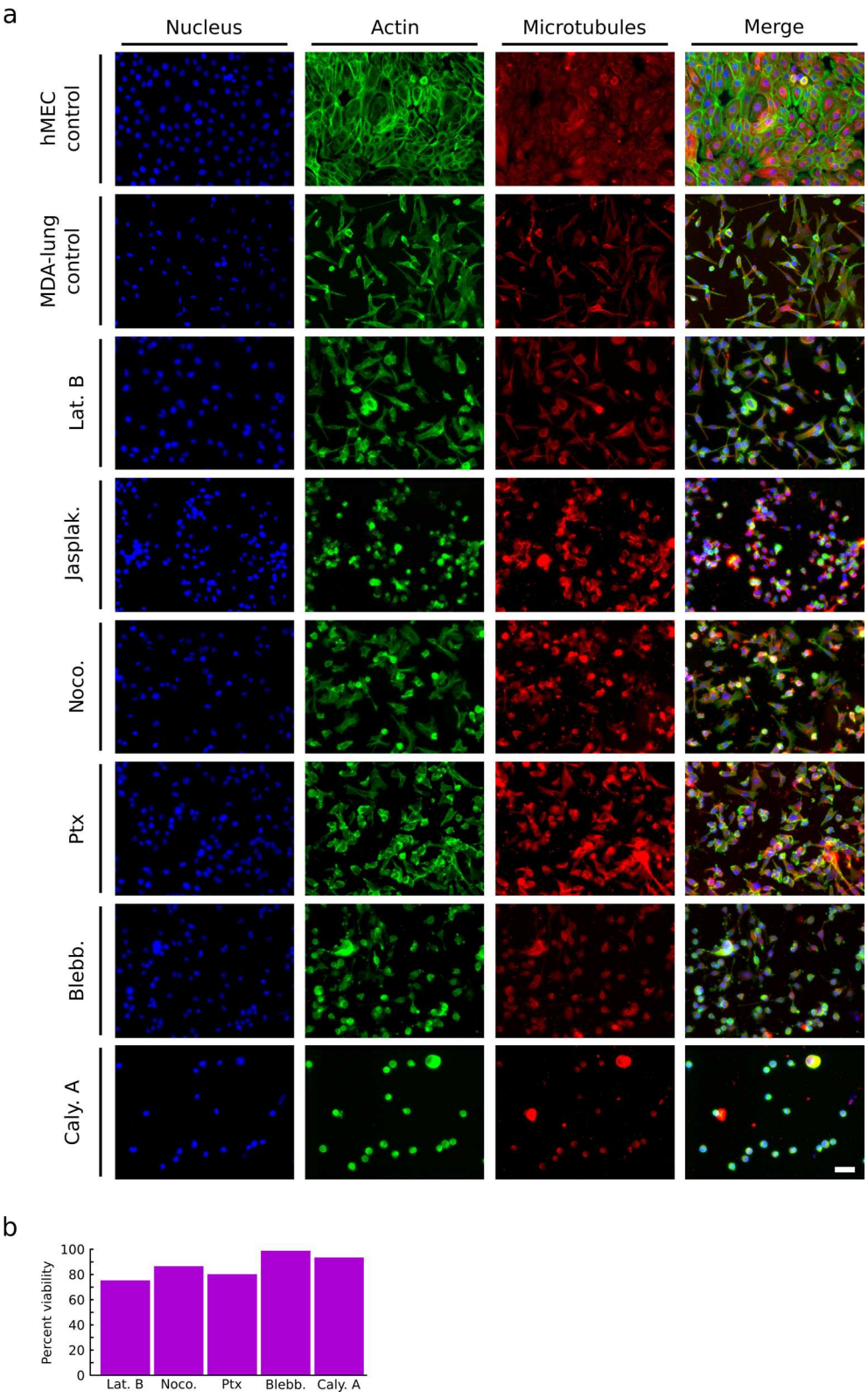

Figure 10: (a) Pharmacological effects of several actin, microtubule, and myosin affecting drugs are shown on MDA-lung cells seeded on a 2D C1 coated surface. Staining for nucleus, actin and microtubules is shown. (b) Viability results are given for MDA-lung cells that were subjected to select drugs. Scale bar is 50 µm.

To test whether degradation of proteins on the bottom surface by cell-secreted enzymes facilitates transhesion to the top surface, we applied a broad spectrum MMP blocker, GM-6001, to the MDA-lung cells. This did not seem to affect transfer, but it also did not dramatically reduce MMPs in the media. Quantification of MMP levels in media reveals a heavy influence of FBS (Fig. 11). Serum starvation of the cells, as well as a combination of serum starvation and GM-6001, did show drastic reduction of MMP activity and did cut the transfer rate dramatically. This reduction did not recover with addition of lysophosphatidic acid, a component in FBS known to stimulate migration[25]. However, due to a multitude of growth factors in FBS, we cannot definitively conclude the role of MMP production independent of other factors in FBS on transhesion.

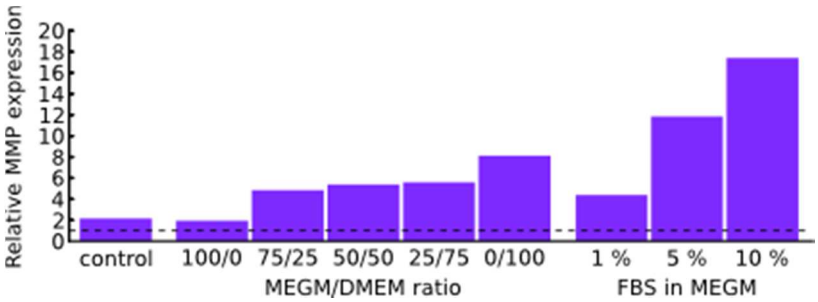

Figure 11: Relative MMP activity of mixtures of MEGM and DMEM, as well as MMP activity in MEGM spiked with varying concentrations of FBS. Control is the fluorescence reading from the MMP assay in PBS. Results show strong correlation of FBS concentration with MMP activity.

3.3 Discussion

Multivariate analyses of phenotypic and genetic biomarkers may provide holistic cellular information that exceeds any single analysis method[26]. The transhesion geometry provides integrative measures of a new set of physical biomarkers that show unique differences for malignant cell lines that have varying tropism to metastatic sites in the brain, lung, and bone. transhesion offers a new dimension of analysis that may better resemble cell environments in the

human body; these cells are continuously exposed to a multitude of ECM proteins across their surfaces, reflecting the environment of a malignant cell migrating through tissue.

The transhesion platform is readily adaptable for a wide range of studies, and facilitates the parallelization of experiments through the multiplexed setup. For all of our studies, we seeded cells on their initial surface for 2 hours, introduced a new surface from above for 3 hours, and maintained a uniform gap distance of 10 microns. These parameters are easily tunable for cells of different sizes and adhesion properties. We tested single ECM proteins in each stripe, but more complex, physiologically relevant mixes of ECM proteins can also be tested (Fig. 12b). Cells experience cues from multiple ECM ligands that can uniquely influence the cell. For instance, it has been shown that C1 prevents fibroblasts from stretching fibronectin (Fn) by stabilizing the conformation of Fn fibers[27]. Another report suggests that while Fn is highly expressed in breast tumors, Fn promotes proliferation while collagen I promotes a stretched morphology, spreading, and adhesion[28].

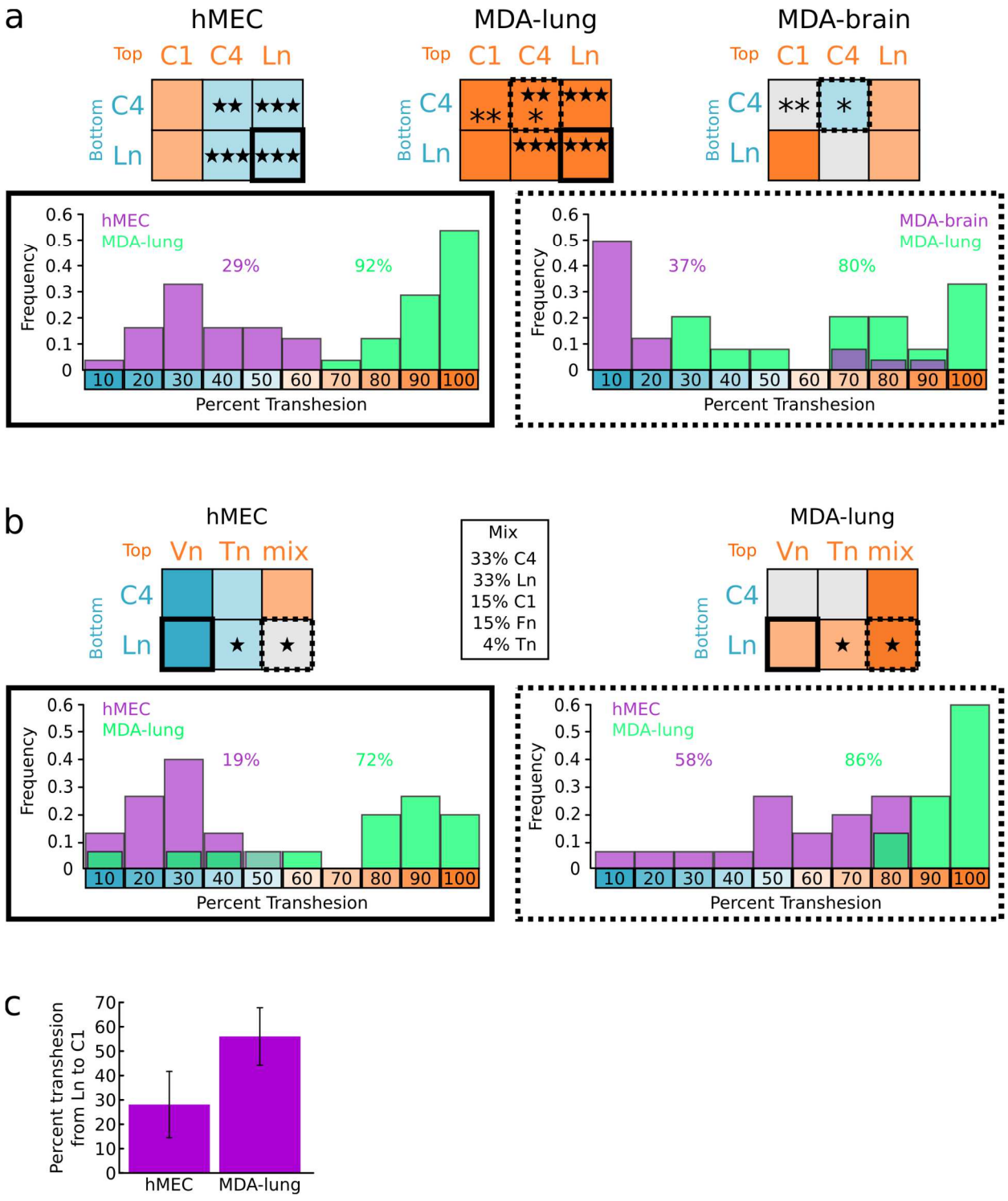

Figure 12: Cell enrichment from a heterogeneous population. (a) Protein pairs that foster distinct transfer behavior between a malignant cell line (MDA-lung) and normal breast line (hMEC) were identified, as well as protein pairs that can further delineate subpopulations of malignant cells (MDA-lung and MDA-brain) that localize to specific secondary sites. n=24. The star symbol is used to show significance between MDA-lung and hMEC, while the asterisk symbol shows significance between MDA-lung and MDA-brain. (b) A complex protein mixture that mimics the ECM mix of lung tissue was tested and compared with individual proteins in their capability to produce distinct adhesive phenotypes between hMEC and MDA-lung. n=12. *P<0.05, **P<0.01, and ***P<0.001. (c) Percent transhesion of a mixed population of hMEC and MDA-lung. Cells were seeded for 2 hours in MEGM media to maintain hMEC viability, and then replaced with DMEM for 2 hours prior to compression.

The hMEC line displays epithelial characteristics, where cell-cell adhesions tend to dominate over cell-ECM protein interactions, especially for apical regions of such polarized epithelial cells. Therefore, ECM signals interacting with these cell surfaces following polarization do not effectively promote migration or adhesion. Interestingly, hMECs appear to form bleb-like protrusions seemingly as a mechanism of cell-sensing, which resembles amoeboid migration as previously reported in fixed height conditions[29]. These protrusions seem to probe the local space for other cells and form cell-cell contacts, which explains the high percentage of nearest neighbors for cells remaining on the bottom surface (Fig. 6).

One of the most striking results is that the malignant cell lines are more likely to transhere, especially if the new surface is coated in C1. MDA preference to a C1 top surface is supported by our observations of increased spreading, as indicated by larger spread area and lower circularity. This behavior is consistent with histology results, which shows that increased expression and remodeling of C1 corresponds to breast cancer progression[22,30–32]. In contrast to hMEC, MDA-MB-231 cells have more mesenchymal features, a phenotype that is associated with increased motility on a 2D surface[33] and in matrigel[34] as individual cells[35]. This may implicate the motile phenotype of mesenchymal cells as a requirement of transhesion, while commitment to the top surface is dependent on the ECM protein type, in this case C1.

Despite such spreading, MDA-lung cells were not found to have punctate focal adhesion staining when examined after transhesion to C1. Conversely, hMEC were observed to have nascent focal adhesions on both the top and bottom surfaces. This is in contrast to 2D cultures, where both cell types can show focal adhesion formation after 1 hour (Fig. 13). In 2D cultures, seeded cells transition from a suspended state to an adhered state, while in our platform, cells start adhered on a surface, but when they transfer they must transition to an adhered state on the

new surface prior to separation. The extended duration of this latter process, as well as having multiple chemical cues of the ECM from opposite surfaces, may delay or prevent focal adhesions from forming in the MDA-lung cells[36].

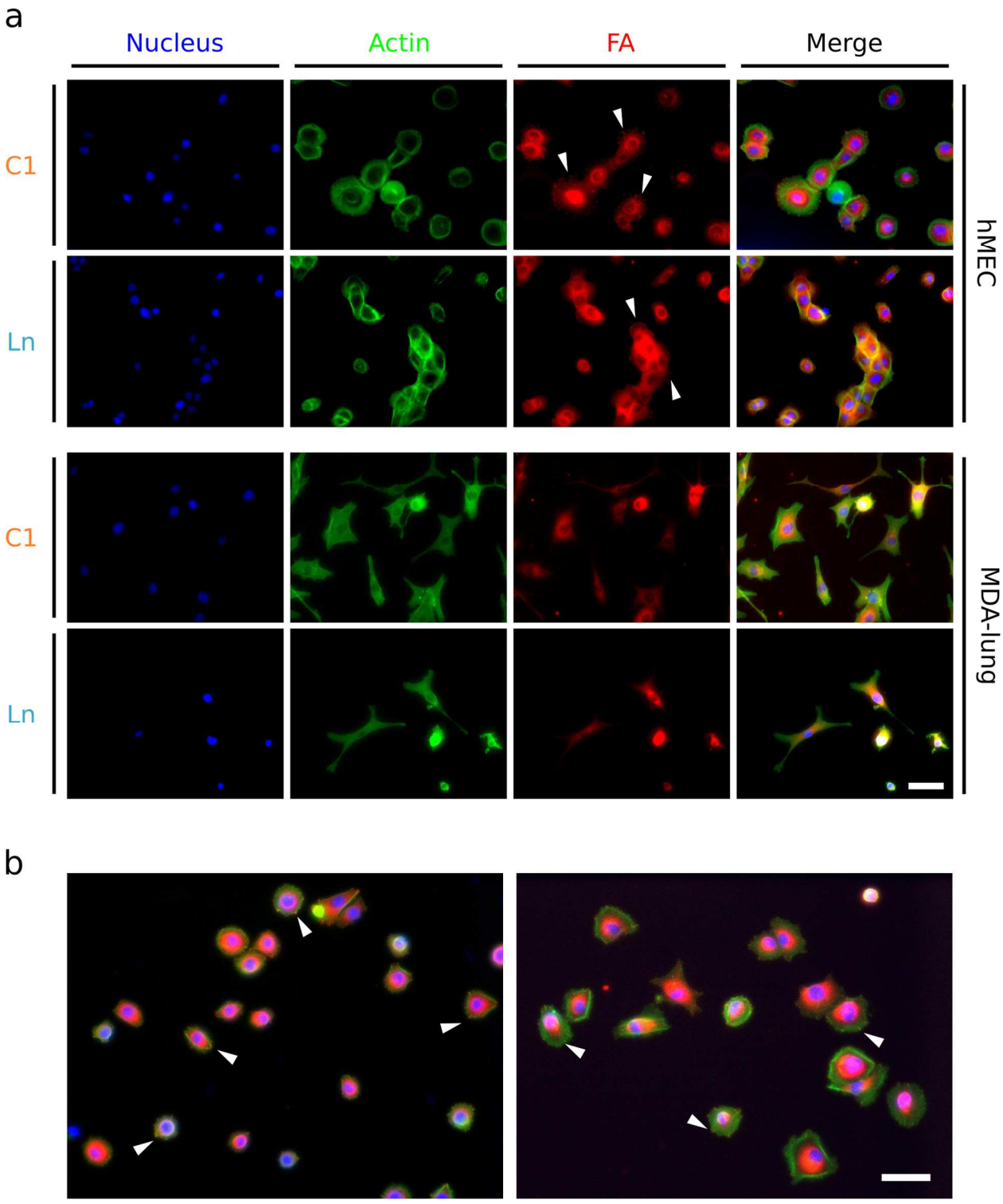

Figure 13: Focal adhesions during transhesion. (a) Confined hMEC and MDA-lung cells were stained for nuclei (DAPI), actin (phalloidin), and focal adhesions (anti-paxillin) after surfaces (C1 top and Ln bottom) were separated. Only hMEC show nascent focal adhesions. This is in contrast to well plates (b), where both cell types form focal adhesions. Scale bar is 50 μm.

The mechanisms supporting transhesion are complex. However, we discovered several key players that appear critical for MDA-lung cells. Since we selected laminin and the collagens for further study, we chose to observe the effects of inhibition on the integrin subunits most closely associated with adhesion to those ECM proteins: α2, α6, and β1. Similarly, other integrins may be interrogated, such as the vitronectin receptor αvβ3, which is widely implicated in cancer progression[6,7,37]. We also tested numerous drugs that affect other cell components involved in the mechanics of cell adhesion: filopodia, actin, microtubules, and myosin. Of these, it seemed that disruption of the actomyosin complex significantly impaired MDA-lung transhesion. Taken together, transhesion in our platform appears to resemble cell migration in 3D environments, where integrin-ECM binding and actomyosin contractility play important roles[36,38].

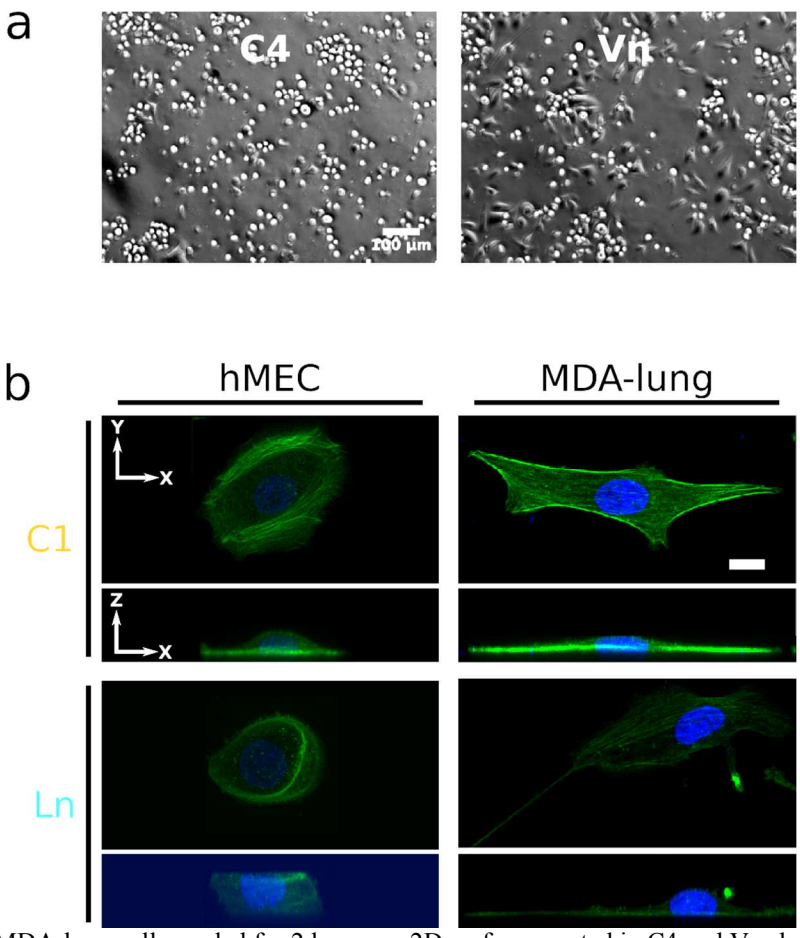

Figure 14: (a) MDA-lung cells seeded for 2 hours on 2D surfaces coated in C4 and Vn show differences in spread area. Scale bar 100 µm. (b) Confocal images show differences in cell spreading on top (C1) and bottom (Ln) surfaces for hMEC and MDA-lung. Scale bar is 10 µm.

When cells were subject to a competition between like proteins (e.g. Fg v Fg) they may transfer at a rate close to 50 % given the geometric symmetry, but interestingly, oftentimes cells strongly favor the top surface or the bottom surface due to other unavoidable asymmetries present in the system. For example, strong adhesion of MDA cells to a bottom Vn-coated surface lead to highly spread morphologies, such that cells no longer possessed sufficient height to make contact with the top surface (Fig. 14a). This reduction in transhesion for such cells is also supported by results showing increased β1 integrin expression for the small subpopulation of MDA-lung cells that remain very spread out on a Ln-coated bottom surface after the majority of cells transfer to a C1-coated top surface (Fig. 14b). Another factor may be differential

degradation of ECM proteins on the initial seeded surfaces, which is largely dependent on the types of MMPs found in the media and expressed by the cells.

Interestingly, when most MDA cell lines are initially seeded on the basement membrane proteins C4 and Ln, they appear to transhere regardless of the protein coated on the opposing top surface. Several sources in the literature suggest multifunctionality in ECM proteins. Malignant breast cells tend to express ADAM-10 and ADAM-17, which can act as both an integrin and a metalloprotease, so they can foster binding and disruption of adhesion[39]. Anti-adhesive effects are seen in several ECM proteins such as thrombospondin[40], tenascin C[41], and laminin[42]. Additionally, cells that are seemingly "repulsed" from the bottom surface may do so because they express MMPs that degrade the proteins patterned on the bottom surfaces. Many malignant cells have also been found to express MMP-2 and MMP-9, which are known to degrade basement membrane proteins like C4 and Ln[43–45]. Because cells interact with the bottom surface for two hours prior to introduction of the top surface, proteins may have degraded to the point where cells find more adhesive ligands on any new surface. Loss of Ln anchoring has previously been linked to aggressive breast cancer[46] but repulsion to a new surface, as shown in our platform, has not been previously demonstrated. Keeping in mind that integrin-ECM interaction can be characterized by recognition, degradation, and stabilization, transhesion fingerprints can generate more holistic phenotypic information about the cells that cannot be observed with other methods that assay expression levels of integrins alone.

This multiplexed tool uniquely characterizes the transhesion of a homogenous cell population, and can later be used as an enrichment platform which enables predictable isolation of subpopulations by the same relative adhesion mechanisms (Fig. 12). Identification of malignant cell populations in tumor biopsies, followed by further delineation of site-specific

metastatic proclivity, may enable early prediction, observation, and treatment of secondary tumors, which are largely responsible for high mortality rates.

Beyond studies of metastatic potential, the transhesion platform can be applied to other cell biology problems, enabled by the design around a standard 60-mm diameter petri-dish. For example, our multiplexed platform can establish differential transhesive fingerprints for induced pluripotent stem cells (iPSCs) and the somatic cells from which they are derived. This may uncover key ECM protein pairs that would allow rare differentiated cells to be extracted from the iPSC culture with the separation platform. By purifying the iPSC culture without bringing them into suspension, we may reduce risks of damage that may be associated with manual processes, enzymatic passaging, or sorting.

3.4 Methods

3.4.1 Photolithography

All wafer molds were developed using standard photolithography methods. New wafers were cleaned with acetone, methanol, and isopropanol. Molds for the glass substrates were created by spinning KMPR 1005 at 5000 rpm and 1000 rpm/s for 30 s to achieve the 5 micron height. Molds for PDMS striping channels required KMPR 1050 spun at 2000 rpm and 1000 rpm/s for 30 s to achieve a ~70 micron height. After soft-baking for 5-7 minutes, wafers were exposed to UV light for 30 s or 3 minutes, respectively, through a photomask. Due to the large features of the photomask, the mask was simply designed in Inkscape and printed on two transparencies in a standard laser printer. The transparencies were first taped together, and then they were taped against a 5” x 5” glass. After exposure, wafers were hard baked for 2 minutes before developing in MF-26A for at least 2 minutes to etch away unpolymerized photoresist. Wafers were baked for 2 minutes, and feature heights were confirmed using a reflectometer

(Nanospec) and profilometer (Dektak). Finally, wafers were exposed to 10 minutes of HMDS coating to render the surfaces hydrophobic.

3.4.2 Glass substrate preparation

1.5" X 1.5" glass squares were cut with a glass cutter from 1.5" X 3" glass slides, and the corners were chipped off to allow the squares to fit comfortably in a 60 mm diameter petri dish. Glass pieces were cleaned with ethanol or isopropanol and mechanical scrubbing. Scotch tape was applied to one side for protection. Laser cut acrylic frames were clipped over the wafers to position glass pieces directly over the patterned regions of the wafer. A drop of PDMS was placed on each of the glass pieces, which were flipped and pressed against the stripe patterns, resulting in a very thin layer (40-60 microns) of patterned PDMS. These were allowed to partially cure at room temperature overnight, followed by full cross-linking in a 60^{o}C oven. The slow partial cure step at room temperature prevents PDMS expansion against the features of the wafer, which facilitates removal. After unclipping the acrylic alignment frames, the glass substrates were removed gently with a razor blade.

3.4.3 PDMS striping channel layer fabrication

PDMS protein striping channels were made using a standard PDMS molding process. Aluminum foil walls were created to contain liquid PDMS. Approximately 25-30 g of PDMS was poured onto the wafer and was degassed in a vacuum chamber for 30 minutes. The PDMS was then cured in a 60 C oven overnight, and was peeled away from the wafer. Using a razor blade, the PDMS was cut around the stripe patterns (channels), and holes were punched for the inlet and outlet of each channel.

3.4.4 Protein coating

The tape on the back of the PDMS-glass pieces was removed, and each substrate was cleaned from dust with tape and isopropanol. A solvent of 95 % ethanol and 5 % water in a beaker was prepared. To this, 1 % glacial acetic acid and 1 % 3-aminopropyltriethoxysilane (APTES) was added, and a magnetic stir bar was used to vigorously mix the solution for 15 minutes. During this time, PDMS-glass pieces were exposed to air plasma (Harrick) for 1 minute at 500 mTorr. These surfaces were immediately submerged in the APTES mixture, and the reaction was set to shake gently on a stir plate for 45 minutes. This rendered the surfaces positively charged, and thereby enabled electrostatic binding of the negatively charged proteins at pH 7.

Protein solutions were simultaneously formulated at 100 μg/mL concentrations. Eight different ECM proteins were patterned (Supplementary Fig. 1b) including the glycoproteins fibronectin (Fn) (Invitrogen) and fibrinogen (Fg) (Sigma), the abundant fibrillar protein collagen I (C1) (Sigma), basement membrane proteins like collagen IV (C4) and laminin (Ln) (Invitrogen), the invasion-mediating protein vitronectin (Vn) (Advanced Biomatrix)[47], the lung invasion-mediating protein tenascin C (Tn) (EMD Millipore)[12], and the bone invasion-mediating protein osteopontin (On) (R&D systems)[11].

After preparing protein solutions, PDMS-glass substrates were washed twice with reagent grade ethanol, air dried, and placed in a fresh petri dish. Each PDMS striping channel was overlaid on a PDMS-glass substrate, and a benchtop magnifying glass was used to align the striping channels with the stripes on the glass. 8 μL of protein solution was injected into each inlet according to the predetermined arrangement of proteins, and was let to sit for 1 hour at

room temperature. Finally, remaining solutions were extracted from each inlet, and the protein striped glass substrates were let to dry overnight at room temperature.

3.4.5 Cell culture

All MDA-MB-231 cell lines, including variants TGL/1833, TGL/4175, and TGL/Brm-2a were cultured in DMEM with 10 % FBS and 1 % Penn/Strep. The hMEC line was cultured using the MEGM bulletkit (Lonza). Upon confluency of approximately 80 %, cells were passaged following traditional techniques. Cells were treated with 0.05 % trypsin to detach them from the culture surface, and were centrifuged at 1,400 rpm. Passage number ranged from 5-30.

3.4.6 Multiplexed cell adhesion assay

All proteins were tested in parallel in the multiplexed format of the assay, in which proteins are patterned in stripes along the 5 micron deep trenches. Upon compression, this format exposed cells to 64 combinations of ECM protein pairs at once for rapid analysis and improved experimental control (Fig. 1d). Stripe cross regions are identified as the regions of interest (Supplementary Fig. 1c). Cells are labeled with Hoechst 33342 nuclear stain, and upon separation they are enumerated to determine their transfer rate in the selected ROIs. A heat map for each cell population with respect to each protein pair are developed to characterize its "relative adhesive landscape", where darker orange indicates greater transfer to the top surface and darker blue indicates proclivity to the bottom surface.

3.4.7 Cell compression

Prior to cell passaging, all surfaces were sterilized in the biosafety cabinet under 15 minutes of UV exposure. 1 mL of cells were passaged and passed through a 40 μm pore size filter to remove cell aggregates before seeding onto the protein-striped substrates at 500,000

cells/mL. Cells were placed in an incubator at 37°C and 5 % CO_2 for 2 hours to adhere to the bottom surface. After this time cells were washed and stained with calcein AM and Hoechst 33342 to stain for live cells and the nucleus, respectively. Bottom surfaces were transferred to a petri dish containing a 1 mm layer of cured PDMS at 40:1 base-to-crosslinker ratio to prevent motion of the glass piece. Similarly, a 1 in x 1 in square 40:1 PDMS piece (thickness 2 mm) was placed between the bottom of the top glass substrate and the top compression plate of the platform. 4 mL of media was added gently over the bottom glass substrate before introducing the top substrate. The top substrate was secured firmly with 4 nuts and bolts. Cells were allowed to sit sandwiched between the two substrates for 3 hours. The 4 nuts and bolts were unfastened, and the top compression plate was gently lifted and submerged in a new petri dish filled with 5 mL of 1XPBS.

3.4.8 Pharmacological studies

All pharmacological studies were performed against a control experiment without inhibitor/drug that verified proper functioning of the platform. MDA-lung cells were treated with one of the following: 6.4 μg/mL rabbit anti-α6 integrin (Abcam, ab84542, lot GR30515), mouse anti-α2 integrin (Abcam, ab55340), rabbit anti-β1 integrin (Abcam, ab134179), 30 μM IPA-3 (Sigma-Aldrich, I2285), 0.1 μM latrunculin B, 1 μM jasplakinolide (Santa Cruz Biotechnology, sc-202191), 20 μM nocodazole (Sigma-Aldrich, M1404), 5 μM paclitaxel, 50 μM blebbistatin (Sigma-Aldrich B0560), 10 nM calyculin A (Sigma-Aldrich C5552), 50 μM GM-6001 (Enzo Life Sciences BML-EI300-0001), and 10 μM lysophosphatidic acid (Sigma L7260). These doses were similar to those used in literature[48–50]. Drugs were incubated for 30 minutes prior to compression.

3.4.9 Imaging

All imaging was performed on a Nikon Ti fluorescence microscope. The platform was first imaged using large scan stitching to identify all ROIs, and the location of the 4 corner alignment marks were identified prior to substrate separation. Substrates were separated and the top compression plate and top substrate were submerged in a new 60 mm diameter petri dish containing PBS to keep the cells viable. After separation, each substrate was positioned according to the location of the alignment marks, and was imaged with large scan stitching.

3.4.10 Image processing

A MATLAB script was developed to identify all ROI and then enumerate cells by Hoechst stain on the bottom and top surfaces of each ROI. Percentage transfer and total cell numbers were calculated for each region.

3.4.11 Immunocytochemistry

Cells were fixed with 4% formaldehyde containing 10 μg/mL Hoechst, 10 mM EDTA, and 5 mM $MgCl_2$ for 15 minutes at 37ºC to cross-link the cells and stain the nuclei. Cells were permeabilized with 0.2% Triton X-100 for 20 minutes. After two PBS washes, substrates were treated with blocking solution (5% goat serum, 1% BSA, and 0.1% v/v Tween 20), followed by primary antibody incubation containing blocking solution with 6.4 μg/mL rabbit anti-α6 integrin (Abcam, ab84542, lot GR30515), mouse anti-α2 integrin (Abcam, ab55340), rabbit anti-β1 integrin (Abcam, ab134179), chicken anti-α-tubulin (Abcam, ab89984, lot GR82981), mouse anti-paxillin (Abcam, ab32084), or mouse anti-E-cadherin (Santa Cruz Biotechnology, sc-21791). Secondary antibody incubation included blocking solution with 1:100 goat anti-chicken AF 568, goat anti-rabbit AF568, goat anti-rabbit AF647, goat anti-mouse AF568, or goat anti-

mouse AF647). Additionally, single-step antibodies and molecules, including phalloidin-AF488, N-cadherin-AF647, and vimentin-AF647, were used in some experiments. Each incubation was done for 1 hour at room temperature, with 2 blocking solution washes in between. Unless otherwise stated, cells on all surfaces had significantly higher integrin expression from the control group, where no primary antibodies were included. HeLa cells were stained with paxillin on a 2D fibronectin-coated surface as a positive control (data not shown).

3.4.12 MMP activity

Cells were dosed with Amplite Universal Fluorimetric MMP activity assay at 2 % v/v for 5 hours. The intensity was measured using a plate reader (Cytation).

3.5 References

1. Paget, S. The distribution of secondary growths in cancer of the breast. *The Lancet* **133,** 571–573 (1889).
2. Togo, S., Shimada, H., Kubota, T., Moossa, A. R. & Hoffman, R. M. ‘ Seed’ to‘ Soil’ is a Return Trip in Metastasis. *Anticancer Res.* **15,** 791–791 (1995).
3. Parker, B. & Sukumar, S. Distant metastasis in breast cancer: molecular mechanisms and therapeutic targets. *Cancer Biol. Ther.* **2,** 13–22 (2003).
4. Weigelt, B., Peterse, J. L. & Van’t Veer, L. J. Breast cancer metastasis: markers and models. *Nat. Rev. Cancer* **5,** 591–602 (2005).
5. Kang, Y. *et al.* A multigenic program mediating breast cancer metastasis to bone. *Cancer Cell* **3,** 537–549 (2003).
6. Felding-Habermann, B. *et al.* Integrin activation controls metastasis in human breast cancer. *Proc. Natl. Acad. Sci.* **98,** 1853–1858 (2001).

7. Liapis, H. M. D., Flath, A. B. S. & Kitazawa, S. M. D. Integrin [alpha]v[beta]3 Expression by Bone-residing Breast Cancer Metastases. *Diagn. Mol. Pathol.* **5,** 127–135 (1996).
8. Minn, A. J. *et al.* Genes that mediate breast cancer metastasis to lung. *Nature* **436,** 518–524 (2005).
9. Cheng, X. & Hung, M.-C. Breast cancer brain metastases. *Cancer Metastasis Rev.* **26,** 635–643 (2007).
10. Bos, P. D. *et al.* Genes that mediate breast cancer metastasis to the brain. *Nature* **459,** 1005–1009 (2009).
11. Ibrahim, T. *et al.* Expression of bone sialoprotein and osteopontin in breast cancer bone metastases. *Clin. Exp. Metastasis* **18,** 253–260 (2000).
12. Oskarsson, T. *et al.* Breast cancer cells produce tenascin C as a metastatic niche component to colonize the lungs. *Nat. Med.* **17,** 867–874 (2011).
13. Gossett, D. R. *et al.* Hydrodynamic stretching of single cells for large population mechanical phenotyping. *Proc. Natl. Acad. Sci.* **109,** 7630–7635 (2012).
14. Otto, O. *et al.* Real-time deformability cytometry: on-the-fly cell mechanical phenotyping. *Nat. Methods* **12,** 199–202 (2015).
15. Hur, S. C., Mach, A. J. & Carlo, D. D. High-throughput size-based rare cell enrichment using microscale vortices. *Biomicrofluidics* **5,** 022206 (2011).
16. Koziol-White, C. J. *et al.* Inhibition of PI3K promotes dilation of human small airways in a rho kinase-dependent manner: PI3K inhibition promotes human airway dilation. *Br. J. Pharmacol.* **173,** 2726–2738 (2016).
17. Barney, L. E. *et al.* A cell–ECM screening method to predict breast cancer metastasis. *Integr. Biol.* **7,** 198–212 (2015).
18. Khalili, A. A. & Ahmad, M. R. A review of cell adhesion studies for biomedical and biological applications. *Int. J. Mol. Sci.* **16,** 18149–18184 (2015).

19. Beningo, K. A., Dembo, M. & Wang, Y. Responses of fibroblasts to anchorage of dorsal extracellular matrix receptors. *Proc. Natl. Acad. Sci.* **101,** 18024–18029 (2004).
20. Fischer, R. S., Myers, K. A., Gardel, M. L. & Waterman, C. M. Stiffness-controlled three-dimensional extracellular matrices for high-resolution imaging of cell behavior. *Nat. Protoc.* **7,** 2056–2066 (2012).
21. Rijal, G. & Li, W. 3D scaffolds in breast cancer research. *Biomaterials* **81,** 135–156 (2016).
22. DuFort, C. C., Paszek, M. J. & Weaver, V. M. Balancing forces: architectural control of mechanotransduction. *Nat. Rev. Mol. Cell Biol.* **12,** 308–319 (2011).
23. Singh, A. *et al.* Adhesion strength-based, label-free isolation of human pluripotent stem cells. *Nat. Methods* **10,** 438–444 (2013).
24. Iuliano, D. J., Saavedra, S. S. & Truskey, G. A. Effect of the conformation and orientation of adsorbed fibronectin on endothelial cell spreading and the strength of adhesion. *J. Biomed. Mater. Res.* **27,** 1103–1113 (1993).
25. Du, J. *et al.* Lysophosphatidic Acid Induces MDA-MB-231 Breast Cancer Cells Migration through Activation of PI3K/PAK1/ERK Signaling. *PLOS ONE* **5,** e15940 (2010).
26. Lee, W. C. *et al.* Multivariate biophysical markers predictive of mesenchymal stromal cell multipotency. *Proc. Natl. Acad. Sci.* **111,** E4409–E4418 (2014).
27. Kubow, K. E. *et al.* Mechanical forces regulate the interactions of fibronectin and collagen I in extracellular matrix. *Nat. Commun.* **6,** (2015).
28. Teng, Y. *et al.* Effects of type I collagen and fibronectin on regulation of breast cancer cell biological and biomechanical characteristics. *J. Med. Biol. Eng.* **34,** 62–68 (2014).
29. Liu, Y.-J. *et al.* Confinement and low adhesion induce fast amoeboid migration of slow mesenchymal cells. *Cell* **160,** 659–672 (2015).
30. Levental, K. R. *et al.* Matrix crosslinking forces tumor progression by enhancing integrin signaling. *Cell* **139,** 891–906 (2009).

31. Ramaswamy, S., Ross, K. N., Lander, E. S. & Golub, T. R. A molecular signature of metastasis in primary solid tumors. *Nat. Genet.* **33,** 49–54 (2003).
32. Wei, S. C. *et al.* Matrix stiffness drives epithelial-mesenchymal transition and tumour metastasis through a TWIST1-G3BP2 mechanotransduction pathway. *Nat. Cell Biol.* **17,** 678–688 (2015).
33. Vuoriluoto, K. *et al.* Vimentin regulates EMT induction by Slug and oncogenic H-Ras and migration by governing Axl expression in breast cancer. *Oncogene* **30,** 1436–1448 (2011).
34. Magee, P., Mcglynn, H. & Rowland, I. Differential effects of isoflavones and lignans on invasiveness of MDA-MB-231 breast cancer cells in vitro. *Cancer Lett.* **208,** 35–41 (2004).
35. Wong, I. Y. *et al.* Collective and individual migration following the epithelial–mesenchymal transition. *Nat. Mater.* **13,** 1063–1071 (2014).
36. Fraley, S. I. *et al.* A distinctive role for focal adhesion proteins in three-dimensional cell motility. *Nat. Cell Biol.* **12,** 598–604 (2010).
37. Sloan, E. K. *et al.* Tumor-specific expression of αvβ3 integrin promotes spontaneous metastasis of breast cancer to bone. *Breast Cancer Res.* **8,** R20 (2006).
38. Petrie, R. J., Koo, H. & Yamada, K. M. Generation of compartmentalized pressure by a nuclear piston governs cell motility in a 3D matrix. *Science* **345,** 1062–1065 (2014).
39. Caiazza, F. *et al.* Targeting ADAM-17 with an inhibitory monoclonal antibody has antitumour effects in triple-negative breast cancer cells. *Br. J. Cancer* **112,** 1895–1903 (2015).
40. Murphy-Ullrich, J. E. & Höök, M. Thrombospondin modulates focal adhesions in endothelial cells. *J. Cell Biol.* **109,** 1309–1319 (1989).
41. Husmann, K., Carbonetto, S. & Schachner, M. Distinct sites on tenascin-C mediate repellent or adhesive interactions with different neuronal cell types. *Cell Commun. Adhes.* **3,** 293–310 (1995).

42. Calof, A. L. & Lander, A. D. Relationship between neuronal migration and cell-substratum adhesion: laminin and merosin promote olfactory neuronal migration but are anti-adhesive. *J. Cell Biol.* **115,** 779–794 (1991).
43. Jones, J. L., Glynn, P. & Walker, R. A. Expression of MMP-2 and MMP-9, their inhibitors, and the activator MT1-MMP in primary breast carcinomas. *J. Pathol.* **189,** 161–168 (1999).
44. Gu, Z. *et al.* A highly specific inhibitor of matrix metalloproteinase-9 rescues laminin from proteolysis and neurons from apoptosis in transient focal cerebral ischemia. *J. Neurosci.* **25,** 6401–6408 (2005).
45. Duffy, M. J., Maguire, T. M., Hill, A., McDermott, E. & O'Higgins, N. Metalloproteinases: role in breast carcinogenesis, invasion and metastasis. *Breast Cancer Res.* **2,** 252 (2000).
46. Akhavan, A. *et al.* Loss of cell-surface laminin anchoring promotes tumor growth and is associated with poor clinical outcomes. *Cancer Res.* **72,** 2578–2588 (2012).
47. Pola, C., Formenti, S. C. & Schneider, R. J. Vitronectin–αvβ3 Integrin Engagement Directs Hypoxia-Resistant mTOR Activity and Sustained Protein Synthesis Linked to Invasion by Breast Cancer Cells. *Cancer Res.* **73,** 4571–4578 (2013).
48. Kraning-Rush, C. M., Carey, S. P., Califano, J. P., Smith, B. N. & Reinhart-King, C. A. The role of the cytoskeleton in cellular force generation in 2D and 3D environments. *Phys. Biol.* **8,** 015009 (2011).
49. Tseng, P., Judy, J. W. & Di Carlo, D. Magnetic nanoparticle–mediated massively parallel mechanical modulation of single-cell behavior. *Nat. Methods* **9,** 1113–1119 (2012).
50. Shankar, J. *et al.* Pseudopodial Actin Dynamics Control Epithelial-Mesenchymal Transition in Metastatic Cancer Cells. *Cancer Res.* **70,** 3780–3790 (2010).

Chapter 4: Conclusion

While new genetic, proteomic, and metabolic techniques are being developed for high content biomarker screening, we propose that cell mechanomics approaches can provide additional information about the cell's physical interaction with microenvironmental properties, which cannot be achieved with molecular analyses. By understanding the biological implications of cell characteristics such as size, deformability, adhesion, migration, and surface expression, as well as characterizing new cell behaviors, we can design diagnostic tools to identify cell populations that exhibit those behaviors. These properties can additionally serve to enrich specific cell subpopulations from background cells

Though significant data and manipulation can be achieved with physical-based tools, it is clear that no single cell property is sufficient to fully characterize or segregate specific cell types. This has led to multivariate analysis protocols to assess several cell properties all at once. For example, Lee et al. predict mesenchymal stem cell multipotency by identifying small, deformable cells showing large nuclear membrane fluctuations[1].

Analyses of multiple physical parameters provides a new dimension of characterizing disease state which, when combined with genetic, proteomic, and metabolic data, can provide a holistic prognosis of patient status.

1. Lee, W. C. *et al.* Multivariate biophysical markers predictive of mesenchymal stromal cell multipotency. *Proc. Natl. Acad. Sci.* **111,** E4409–E4418 (2014).